

A Spitzer Study of Comets 2P/Encke, 67P/Churyumov-Gerasimenko, and C/2001 HT50 (LINEAR-NEAT)

Michael S. Kelley,¹ Charles E. Woodward,¹ David E. Harker,² Diane H. Wooden,³ Robert D. Gehrz,¹ Humberto Campins,⁴ Martha S. Hanner,⁵ Susan M. Lederer,⁶ David J. Osip,⁷ Jana Pittichová,^{8,9} and Elisha Polomski¹

msk@astro.umn.edu

ABSTRACT

We present infrared images and spectra of comets 2P/Encke, 67P/Churyumov-Gerasimenko, and C/2001 HT50 (LINEAR-NEAT) as part of a larger program to observe comets inside of 5 AU from the sun with the *Spitzer Space Telescope*. The nucleus of comet 2P/Encke was observed at two vastly different phase angles (20° and 63°). Model fits to the spectral energy distributions of the nucleus suggest comet Encke's infrared beaming parameter derived from the near-Earth asteroid thermal model may have a phase angle dependence. The observed emission from comet Encke's dust coma is best-modeled using predominately amorphous carbon grains with a grain size distribution that peaks near 0.4 μm , and the silicate contribution by mass to the sub-micron dust coma is constrained to $< 31\%$. Comet 67P/Churyumov-Gerasimenko was observed with distinct coma emission in excess of a model nucleus at a

¹Department of Astronomy, University of Minnesota, 116 Church St SE, Minneapolis, MN 55455

²Center for Astronomy and Space Science, University of California, San Diego, 9500 Gilman Drive, Department 0424, San Diego, CA 92093

³NASA Ames Research Center, Space Science Division, MS 245-3, Moffett Field, CA 94035

⁴Department of Physics, University of Central Florida, Orlando, FL 32816

⁵Department of Astronomy, University of Massachusetts, 710 North Pleasant Street, Amherst, MA 01003

⁶Department of Physics, California State University, 5500 University Parkway, San Bernardino, CA 92407

⁷Las Campanas Observatory, Carnegie Observatories, Casilla 601, La Serena, Chile

⁸Institute for Astronomy, University of Hawaii at Manoa, 2680 Woodlawn Drive, Honolulu, HI 96822

⁹Astronomical Institute, Slovak Academy of Sciences, Dubravska cesta 9, 845 04 Bratislava, Slovak Republic

heliocentric distance of 5.0 AU. The coma detection suggests that sublimation processes are still active or grains from recent activity remain near the nucleus. Comet C/2001 HT50 (LINEAR-NEAT) showed evidence for crystalline silicates in the spectrum obtained at 3.2 AU and we derive a silicate-to-carbon dust ratio of 0.6. The ratio is an order of magnitude lower than that derived for comets 9P/Tempel 1 during the *Deep Impact* encounter and C/1995 O1 (Hale-Bopp).

Subject headings: Comets: Individual (2P/Encke, 67P/Churyumov-Gerasimenko, C/2001 HT50 (LINEAR-NEAT)), Infrared: Solar System

1. INTRODUCTION

Comets are frozen reservoirs of primitive solar dust grains and ices. Analysis of the composition and size distribution of cometary dust grains from infrared imaging and spectroscopic observations expedites an appraisal of the physical characteristics of the solid materials that constituted the primitive solar nebula (A’Hearn 2004; Ehrenfreund et al. 2004; Wooden et al. 2005). The study of comets is an indirect probe of the origin of the constituents of the primitive solar system, their subsequent evolution into planetesimals, and their relationship to materials in other astrophysical environments (Wooden et al. 2005).

Although comets of all types have undergone some amount of post-formation processing, they remain the best preserved sources of material extant during our solar system’s epoch of planet formation. In the current paradigm, the nearly isotropic comets (i.e., Oort cloud and Halley-type comets) formed amongst the giant planets and were scattered into large orbits, in a spherically symmetric manner (Dones et al. 2004). The ecliptic comets (including Jupiter-family comets) originate from the Kuiper-belt and scattered disk populations and likely formed *in situ* or in the transneptunian region (Duncan et al. 2004; Morbidelli & Brown 2004). Comparisons between the nearly isotropic and ecliptic comets may reveal the differences in their post-formation processing or the structure and mineralogy of the proto-planetary disk. Both nearly isotropic and ecliptic comets have been exposed to bombardment by UV photons and cosmic rays, although to varying extents (the Jupiter-family comets have been exposed to $\sim 10^5$ times more UV and 100 KeV solar cosmic rays than the Oort cloud comets). The ecliptic comets have suffered frequent collisions during their residence in the Kuiper-belt and are likely to be fragments of larger Kuiper-belt bodies (Stern 2003). The number of comets studied by mid-infrared spectroscopic methods necessary to determine their detailed mineralogies is increasing (e.g., see Hanner et al. 1996; Harker et al. 2006, 2005, 2002, 1999; Honda et al. 2004; Kelley et al. 2005b; Lynch et al. 2002, 2000; Sitko et al. 2004; Wooden et al. 2004) and we may soon be able to compare comets to each other as

groups, rather than individually.

We present *Spitzer Space Telescope* (Werner et al. 2004) images and spectra of comets 2P/Encke, a 3.3 yr period (P), Jupiter-family comet with a perihelion distance, $q = 0.3$ AU, known for an abundance of large dust particles (Reach et al. 2000) and an extensive debris trail (Sykes & Walker 1992); 67P/Churyumov-Gerasimenko (67P), $P = 6.6$ yr, $q = 1.3$ AU, a Jupiter-family comet and the primary mission target of the European Space Agency’s *Rosetta* spacecraft; and C/2001 HT50 (LINEAR-NEAT) (HT50), a long period, Oort cloud comet, $P = 40,250$ yr, $q = 2.8$ AU.

Comet Encke frequently approaches the Earth on its 3.3 yr orbit and is one of the most studied of all comets (Sekanina 1991). Comet Encke was also one of the first comets discovered to have a dust trail (Sykes & Walker 1992). Dust trails are composed of large ($\gtrsim 0.1$ mm), slow moving particles and are precursors to meteor streams [Encke is associated with the Taurid meteor stream (Whipple & Hamid 1950)]. The comet also exhibits weak or non-existent $10 \mu\text{m}$ silicate emission (Campins et al. 1982; Gehrz et al. 1989; Lisse et al. 2004). The existence of a dust trail, association with a meteor stream, and the lack of a strong silicate feature has led investigators to conclude that Encke’s dust production is dominated by large particles. We present *Spitzer Space Telescope* observations of comet Encke in §2.1, and derive the comet’s dust coma mineralogy at 2.4 AU in §3.1.2. The mineralogy of comet Encke is discussed in §4.2. We derive the temperature and effective size of the nucleus of comet Encke in §3.1.1 and discuss the results in §4.1.

Comet 67P is the primary target of the *Rosetta* mission. The spacecraft is designed to intercept and orbit the comet at $r_h = 4.5$ AU (pre-perihelion) to study the development of coma activity as the comet approaches the sun¹. Information on the comet’s dust environment is crucial to mission planning, which motivated our *Spitzer* observations of the comet at 5.0 AU (post-perihelion). The observation is presented in §2.1 and the results presented in §3.2.

Comet HT50 is an Oort cloud comet with an orbital period that suggests it has orbited the sun many times ($P = 40,250$ yr). It was discovered to be cometary at the large heliocentric distance of 7.5 AU (Pravdo et al. 2001). We observed comet HT50 twice with *Spitzer*. Both observations are presented in §2.1 and we derive dust mineralogies at both epochs in §3.3. We discuss HT50’s mineral content and compare it to other Oort cloud comets in §4.2.

¹<http://www.esa.int/esaMI/Rosetta/>

2. OBSERVATIONS AND REDUCTION

2.1. Spectra

Spectra of comets Encke, 67P, and HT50 were obtained with the Infrared Spectrograph (IRS) instrument (Houck et al. 2004) on *Spitzer*. All comets were observed in both low- ($R \approx 64$ –128) and high- ($R \approx 600$) resolution modes, although not at all wavelengths. The slit widths, aperture extraction sizes (described below), and slit orientations are listed in Table 1. Note that the slit parameters force us to sample different areas of each comet’s coma (even though each slit extraction is centered on the nucleus) and remain as a source of unknown error in our resultant spectra. A summary of our observations is presented in Table 2. There were two observations of comet Encke, one from our *Spitzer* guaranteed time observation (GTO) program, program identification (PID) 119, and one from PID 210, one of comet 67P from our general observer proposal (PID 2316), and two temporally distinct observations of HT50 from our GTO program (PID 131).

Post-pipeline spectral reductions were performed on IRS pipeline S12.0.2 basic calibrated data (BCD) frames. Our reduction method proceeded as follows: 1) The BCD frames were two-dimensionally background subtracted (when possible, as described below) and fatally bad pixels were removed by nearest-neighbor interpolation. 2) Spectral extraction and initial calibration were performed by the *Spitzer* IRS Custom Extraction (SPICE) tool, available from the SSC². If a two-dimensional background subtraction was not possible, we subtracted a background model from the extracted spectra at this step. 3) We removed the nucleus contribution, if known, from the extracted spectra. Nuclei were modeled with the near-Earth asteroid thermal model (Harris 1998; Delbó & Harris 2002) as described in §3.1.1. 4) We corrected the combined, nucleus subtracted spectra with our derived extended source calibration (described below). 5) We scaled each module to produce one continuous spectrum. The scaling removed module-to-module mis-calibrations and corrected for differences in module slit orientations with respect to the comet comae. 6) Finally, we scaled the entire spectrum to agree with aperture photometry derived from *Spitzer* imaging (§2.2), if possible.

All spectra were extracted with a constant width aperture to produce a final spectrum representative of a given aperture size around the comet (Table 1). Our SL and LL apertures were 17.5'' and 51.5'' on the sky ($\approx 1/3$ of the slit), i.e., they encompass the first diffraction ring of a point source at the longest wavelength of each module. The default point source optimized aperture used by the IRS calibration pipeline has an aperture size that varies with

²Available at <http://ssc.spitzer.caltech.edu/postbcd/>

wavelength, i.e., the default aperture width in arc seconds is proportional to wavelength. Such an aperture encompasses a diffraction limited point source (but a varying amount of sky) at every extracted wavelength. Therefore, the point source optimized aperture is not optimized for extended source extractions. We compared spectra of the IRS calibration star HD 173511 extracted with our constant width apertures to spectra extracted with the default point source tuned apertures. The differences in the point-to-point photometry (aperture averaged at a given wavelength) between the two spectra were $\lesssim 2\%$. We note the IRS pipeline uses the entire available slit by default in the high-resolution modules.

An automated spectral calibration of extended sources was not available from the SSC, yet the extent of the comae of Encke and HT50 (described below) requires us to calibrate these spectra for extended sources. Currently, point sources are used for IRS calibration targets. We estimate the narrow entrance slits of the IRS modules block up to 40% of the flux of a point source at the longest wavelengths. Although this does not introduce additional absolute photometric uncertainty into the final data products when calibrating point sources (as this same fraction is always removed from all point sources), the slit-loss does affect the photometric precision for sources larger than the point spread function of the instrument. The emission from comets is comprised of emission from the nucleus (generally spatially unresolved) plus a contribution from the coma, which is a region of radially and azimuthally varying surface brightness. To correctly flux calibrate the comet spectra, the nucleus spectrum must be subtracted if the nucleus flux is a significant fraction of the total emission in the slit (step 3, above). Inspection of the IRS peak-up images is used to confirm the validity of this assumption for any individual comet (cf, §2.2). Comets Encke and 67P required nucleus subtraction, HT50 did not. The Encke nucleus is discussed in §3.1.1 and the 67P nucleus is discussed in §3.2. In all cases, we assume the coma surface brightness is a slowly varying function over the slit width (again confirmed by the peak-up images). Next, we generate an image of a point source at each extracted wavelength for an obscured primary with *Spitzer*'s optical parameters (Werner et al. 2004). A slit mask is applied to the image and the flux in the slit mask (I_λ) is compared to the total flux of the simulated point source ($I_{\lambda,0}$). The slit-loss correction factor is $1 - I_\lambda/I_{\lambda,0}$ (Fig. 1). The coefficients of third-order polynomial fits to the slit-loss correction factors (λ in units of μm) for the four IRS modules are given in Table 3. This slit-loss correction factor is multiplicatively applied at each wavelength to the nuclear flux subtracted spectra.

The five observations (Table 2) were designed with various observing strategies. The first observation of Encke (PID 119, AORKEY 6582016) was designed to obtain high-resolution spectra of the comet from 10–38 μm and low-resolution spectra from 5–14 μm . It was executed on 2004 June 25 at 05:28 UT when Encke was at a heliocentric distance, r_h , of 2.573 AU, a *Spitzer*-comet distance, Δ_s , of 1.985 AU, and a phase angle, ϕ , of 21° . The

observation used an IRS spectral map astronomical observing request (AOR). We describe spectral map AORs with $n_{\parallel} \times n_{\perp}$ notation, where n_{\parallel} is the number of steps parallel to the slit’s long (spatial) direction, and n_{\perp} is the number of steps perpendicular to the long direction. The first comet Encke observation used a 1×3 map of $60''$ steps perpendicular to the slit direction for all three modules. The two $60''$ steps off-source provide background measurements for the on-source position. A red peak-up image was used to acquire comet Encke and center the IRS slits.

The second observation of Encke (PID 210, AORKEY 6613248) only used low-resolution modules to cover the entire $5\text{--}38 \mu\text{m}$ spectral region and was executed on 2004 June 25 at 08:27 UT ($r_h = 2.577$ AU, $\Delta_s = 1.982$ AU, $\phi = 21^\circ$). A blue peak-up image was used to acquire comet Encke. The AOR for the $5\text{--}14 \mu\text{m}$ low-resolution module (SL) executed a 2×1 spectral map with $20''$ steps parallel to the slit and the $14\text{--}38 \mu\text{m}$ low-resolution module (LL) executed a 3×1 map with $40''$ steps parallel to the slit. The parallel motion was small enough such that the comet was located in the slit for each map position.

Each low-resolution module consist of two slits, one of which is centered on the science target and the other offset $\approx 60''$ for SL and $\approx 90''$ for LL from the comet (Fig. 2). We use the extra slit position to background subtract our spectra. For example, when the comet is in the 1st order SL slit (SL1, $7\text{--}14 \mu\text{m}$), sky background is measured in the 2nd order SL slit (SL2, $5\text{--}7 \mu\text{m}$). The spacecraft is nodded to place the comet in the SL2 slit, providing a measurement of the sky background in SL1 (see Fig. 2). For the second observation of comet Encke, the off-source order is used as a background measurement and two-dimensionally subtracted from the science order.

The observation of comet 67P (PID 2316, AORKEY 10204928) used an IRS spectral stare AOR in both long wavelength modules and resulted in a spectrum spanning $14\text{--}38 \mu\text{m}$. This AOR was executed on 2004 July 15 at 08:13 UT ($r_h = 4.987$ AU, $\Delta_s = 4.744$ AU, $\phi = 12^\circ$). The red peak-up array shows a point source at the location of the comet. To remove the background in LL, we subtracted nod pairs and extracted the resulting spectra. The high-resolution module did not detect the comet and will no longer be discussed.

Two observations of comet HT50 were executed. The first observation, obtained on 2003 December 17 at 15:39 UT ($r_h = 3.238$ AU, $\Delta_s = 2.652$ AU, $\phi = 16^\circ$), was an IRS spectral map AOR (PID 131, AORKEY 6589440) of size 1×3 with $7.2''$ steps (\perp) SL, a 2×3 map of $7.0'' \times 4.8''$ ($\parallel \times \perp$) for the short wavelength, high-resolution module (SH), and a 2×3 map of $12.8'' \times 9.6''$ ($\parallel \times \perp$) for the long wavelength, high-resolution module (LH). We extracted spectra from the map positions with the greatest amount of signal. The second observation (PID 131, AORKEY 11625472) was obtained on 2004 July 18 at 10:36 UT ($r_h = 4.598$ AU, $\Delta_s = 4.368$ AU, $\phi = 13^\circ$) with an IRS spectral stare AOR for

both high-resolution modules and the first order (7–14 μm) of the SL module. There were no measurements of the background for the SH and LH modules. Instead, the background flux density was estimated using the background model in the *Spitzer Planning Observations Tool* (SPOT) provided by the *Spitzer* Science Center (SSC)³. The model background was subtracted after spectral extraction. Restricting the second epoch SL observation of HT50 to a one order spectral stare does not permit us to use the same two-dimensional background subtraction techniques employed for comet Encke. Furthermore, the extent of the coma in HT50 does not permit us to directly nod subtract the images to remove the background as described above for comet 67P (67P was a point source within the slit). However, the SL module is long enough in the spatial dimension ($\approx 60''$ long) such that the coma of HT50 did not entirely fill the slit. To determine the background contribution in SL, a Gaussian plus linear background term was fitted to the spatial dimension for every λ_i . The linear background term was subtracted from the extracted spectrum.

2.2. Imaging

All comets were imaged at the time of spectra acquisition by the peak-up mode of the IRS. Comet Encke was also observed with the Infrared Array Camera (IRAC) in all band-passes during *Spitzer's* in-orbit checkout and science verification phase (W. T. Reach et al. 2006, in preparation) on 2003 November 11 at 17:33 UT ($r_h = 1.094$ AU, $\Delta_s = 0.232$ AU, $\phi = 63^\circ$). The 8.0 μm images saturated on the nucleus, but the remaining short exposure (0.6 s) 3.6–5.8 μm IRAC images did not saturate and were used in our analysis (Fig. 3). Encke was again imaged with IRAC during normal science operations (PID 119, AORKEY 6581760) on 2004 June 29 at 22:05 UT ($r_h = 2.611$ AU, $\Delta_s = 1.958$ AU, $\phi = 22^\circ$) and with the Multiband Imaging Photometer for *Spitzer* (MIPS) at 24 and 70 μm (PID 119, AORKEY 6582272) on 2004 June 23 at 05:04 UT ($r_h = 2.556$ AU, $\Delta_s = 1.997$ AU, $\phi = 20^\circ$; Fig. 4). Detailed information regarding the performance and use of IRAC and MIPS is provided by Fazio et al. (2004) and Rieke et al. (2004), respectively. The imaging observations are summarized in Table 4. The 2003 November data were processed with IRAC pipeline S11.0.2 and the 2004 June data were processed with IRAC and MIPS pipelines S11.4.0.

The 2004 June comet Encke images were mosaicked in the rest frame of the comet with the MOPEX software (Makovoz & Khan 2005) at the native IRAC and MIPS scales (1.22'' pixel⁻¹ for IRAC, 2.5'' pixel⁻¹ for MIPS 24, and 5.1'' pixel⁻¹ for MIPS 70) and are presented in Fig. 4. The nucleus clearly dominates the 5.8, 8, and 24 μm images based

³Available at <http://ssc.spitzer.caltech.edu/propkit/spot/>

on the tenuous coma emission and distinct diffraction rings. Careful inspection also reveals that the nucleus is detected at 3.6, 4.5, and 70 μm . Comet Encke’s debris trail is seen as a diagonal line of emission extending across the 8 and 24 μm images (Gehrz et al. 2006). Also evident are two streaks of material that comprise the remains of Encke’s activity during this perihelion passage.

The IRS peak-up images are presented in Fig. 5. All images use the red peak-up array ($\lambda_c = 22 \mu\text{m}$) except the 2004 June 25 08:27 UT Encke peak-up, which uses the blue peak-up array ($\lambda_c = 16 \mu\text{m}$). The images are not flux calibrated but are useful in describing the comet morphologies in the following sections.

3. RESULTS AND MODELS

3.1. 2P/Encke

3.1.1. *The Nucleus and the NEATM*

The spectrum of the Encke nucleus must be estimated and subtracted from the raw comet spectrum before extended source calibration, as discussed in §2.1. The light from a comet nucleus is a combination of reflected light and thermal emission at the shortest wavelengths ($\lesssim 5 \mu\text{m}$) and solely comprised of thermal emission at longer wavelengths ($\gtrsim 5 \mu\text{m}$). We approximate the reflected solar spectrum with a 5770 K black body. The thermal emission for comet nuclei is typically modeled with asteroid thermal models (Campins et al. 1987; Veeder et al. 1987; Fernández et al. 2000; Stansberry et al. 2004), which have consistently modeled the thermal emission from those comets visited by spacecraft, for example 9P/Tempel 1 (Lisse et al. 2005; Harker et al. 2005) and 81P/Wild 2 (Fernandez 1999). Originally, the standard thermal model (STM) was successful in modeling the thermal emission from asteroids at small ($\leq 30^\circ$), phase angles (Lebofsky et al. 1986). Harris (1998) proposed the near-Earth asteroid thermal model (NEATM) that extends the STM to higher phase angles and introduces a variable infrared (IR) beaming parameter, η , rather than holding it constant at 0.756; a value which reproduces the diameters of asteroids Ceres and Pallas (Lebofsky et al. 1986). The IR beaming parameter in models either raises or lowers the sub-solar temperature, T_{ss} , as

$$T_{ss} = \left[\frac{(1 - A)S}{\eta\epsilon\sigma} \right]^{1/4} \text{ (K)}, \quad (1)$$

where A is the bolometric bond albedo, S is the incident solar flux, ϵ is the infrared emissivity, and σ is the Stefan-Boltzmann constant. In our treatment, a scaled 5770 K black body

spectrum was added to account for any reflected light at the shortest wavelengths ($\lesssim 5 \mu\text{m}$),

$$F_\lambda = \frac{\alpha \pi B_\lambda(5770 \text{ K}) R^2 R_\odot^2}{4 \Delta^2 r_h^2} (\text{W cm}^{-2} \mu\text{m}^{-1}), \quad (2)$$

where α is freely variable, unit less scale parameter, πB_λ is the Planck function in $\text{W cm}^{-2} \mu\text{m}^{-1}$, R is the radius of the comet in km, R_\odot is the radius of the sun in km, Δ is the comet-observer distance in km, and r_h is the comet-sun distance in km.

The near diffraction limited *Spitzer* images of comet Encke can be used to estimate the size of the comet nucleus if the coma contribution to the observed surface brightness is negligible or can be removed. In the two sets of IRAC images and the MIPS 70 μm image (Fig. 3 and 4), the coma was faint or undetected and the nucleus was sufficiently measured through aperture photometry. Aperture corrections from the IRAC Data Handbook were applied to the IRAC photometry to account for the chosen aperture radii and background annuli [IRAC is calibrated with a 10 pixel radius aperture and a 10–20 pixel annulus, (Spitzer Science Center 2006a)]. Aperture corrections applied to the MIPS photometry were derived from the 500 K MIPS point source response functions provided by the SSC³. All apertures were 5–10 pixels in radius except for the 2004 June IRAC 3.6 and 4.5 μm apertures, which were set to 2 pixels in radius to avoid neighboring stars. The MIPS 24 μm image was fitted with a point source derived from stars in the field and the IRAC 8 μm image was saturated by the nucleus. The measured fluxes are provided in Table 5. The current estimate of the flux calibration errors is $\approx 2\%$ for IRAC (Reach et al. 2005) and $\approx 10\%$ and $\approx 20\%$ for MIPS 24 and 70 (Spitzer Science Center 2006b). The errors in Table 5 were produced from the quadrature addition of the formal photometric errors and the flux calibration errors.

The IRAC color corrections to the photometry are very sensitive to the underlying spectral energy distribution (SED) when dealing with black bodies in the 200–400 K range, e.g., the 3.6 μm color correction varies from 6–51% for $T = 400\text{--}200$ K (Spitzer Science Center 2006a). Additionally, the 3.6 μm bandpass likely includes an equal combination of thermal emission and reflected solar radiation from the nucleus ($\approx 50\%$ from each) [e.g., the SED of comet C/1995 O1 (Hale-Bopp)—(Harker et al. 2002)]. We fit the SED with an initial NEATM model to approximate the true SED and calculate color corrections as prescribed in the IRAC Data Handbook (Spitzer Science Center 2006a).

The color corrected SEDs were modeled with a non-linear reduced chi-squared (χ_ν^2) fitting routine using the NEATM to derive the effective radius of comet Encke’s nucleus. The 2004 June epoch had the best spectral coverage, ranging from 3.6–70 μm . Three parameters affect the color-temperature of the nucleus, ϵ , A , and η . For Encke’s nucleus, we

³Available at <http://ssc.spitzer.caltech.edu/mips/psffits/>.

varied η as a free parameter, adopted a geometric albedo, $p_v = 0.047$, which is related to the Bond albedo (Hanner et al. 1981), following the discussion by Fernández et al. (2000), and set $\epsilon = 0.9$. The best-fit effective radius was $R = 2.34 \pm 0.14$ km ($\eta = 0.735 \pm 0.046$, $\chi_\nu^2 = 3.5$). The entire list of fitted parameters is presented in Table 6 and the model SED is presented in Fig. 6.

The 2003 November SED was limited in spectral coverage to 3.6–5.7 μm and the number of photometry points (3) permitted us to only fit two parameters at a time. Therefore, we fixed the value of η to the best-fit value derived from the 2004 June epoch and fitted R and the scale parameter of the reflected light (α). The result was an effective nucleus radius of 1.72 ± 0.10 km with $\chi_\nu^2 = 11.6$. The error was derived by varying η over the 2004 June range of ± 0.046 . The fit is presented in Table 6 and the SED in Fig. 7.

The 2003 November and 2004 June best-fit effective nucleus radii are different by 0.6 km. If this is evidence for a non-spherical nucleus then the axial ratio is at least $a/c = 1.4$. This value is consistent with the Fernández et al. (2000) axial ratio of $a/c \geq 2.6$ derived from the visual light curve of the nucleus. Our *Spitzer* observations were separated by seven months, however, we can not reliably re-phase our data as the rotation period of Encke’s nucleus is not precisely known (Fernández et al. 2005; Harmon & Nolan 2005). Previous investigations of comet Encke’s nucleus with thermal observations provide effective radii consistent with our derived value of 2.34 ± 0.14 km. Fernández et al. (2000) derive a value of $R = 2.4 \pm 0.3$ km, Gehrz et al. (1989) posit $R = 2.5\text{--}6.4$ km, and Campins (1988) conclude $R < 2.9$ km.

The 0.6 km effective radius disagreement in our *Spitzer* estimates can be minimized by varying η in the 2003 November fits and forcing the radius to be constant at 2.34 km. This method results in $\eta = 1.026 \pm 0.061$ and $\chi_\nu^2 = 0.11$. The new fit is presented in Table 6 and in Fig. 7. The low χ_ν^2 indicates an under-constrained fit, but the fit appears improved as the scattered light contribution in the model SED is similar to the 2004 June best-fit (Fig. 6). Recent work on near-Earth asteroids suggests η may have a phase angle dependence (Delbó et al. 2003; Wolters et al. 2005). We discuss the radius of comet Encke and the role of the IR beaming parameter further in §4.1.

3.1.2. The Coma and the Dust Thermal Model

To properly model and interpret the coma dust emission in comet Encke requires a useful photometric calibration of the narrow slit spectra. First, we must take into account the varying slit widths amongst the IRS modules (ranging from 3.7'' to 11.1''), normalizing to an aperture size of radius 4.5''. Our adopted aperture size is roughly equivalent in area to the

module with the smallest slit and extraction aperture (SL), which is $3.7'' \times 17.5''$ as described above (§2.1). Note that the aperture normalization cannot account for the different regions sampled by the different slit sizes and orientations (§2.1).

Small pointing offsets will cause mis-calibrations of the spectral flux, especially with the SL module, which has a slit width of $3.7''$. This effect is evident when we consider that the inner peak of the *Spitzer* point spread function (PSF) has a full-width at half-maximum of about $2.4''$ at $10 \mu\text{m}$. The coma flux can be estimated from the MIPS $24 \mu\text{m}$ image where we have subtracted the nucleus. The resultant flux can then be used to photometrically calibrate all spectra through module-to-module wavelength overlaps. We measure the coma flux using two methods. Aperture photometry (Method 1) on the residual coma of the point source subtracted image yields a coma flux density of $3.36 \pm 0.20 \times 10^{-21} \text{ W cm}^{-2} \mu\text{m}^{-1}$ in a $4.5''$ radius (1.8 pixels) beam. The error includes the photometric uncertainty of the nucleus subtraction assuming it is distributed evenly over the PSF. Alternatively (Method 2), we fit the azimuthally averaged aperture flux density profile from 3–12 pixels in radius with a power-law, $F(\rho) = C\rho^k$, where C is a scale factor to account for the total brightness, ρ is the aperture radius in pixels, and k is the logarithmic slope. Our fit yields the values $C = 1.46 \pm 0.03 \text{ W cm}^{-2} \mu\text{m}^{-1}$ and $k = 1.509 \pm 0.009$ ($\chi^2_\nu = 0.8$). The best-fit slope is different than the nominal “steady-state” profile ($\rho^{1.0}$, Jewitt 1991) because of the highly structured dust morphology of comet Encke at this epoch and these aperture radii (see Fig. 4). Computing the flux enclosed in a $4.5''$ radius aperture with this surface brightness profile yields a coma flux density of $3.55 \pm 0.18 \times 10^{-21} \text{ W cm}^{-2} \mu\text{m}^{-1}$, again including the PSF fit error. The two methods are in good agreement. We elect to adopt Method 2 for scaling the IRS spectra as it is less likely influenced by the pixel-to-pixel errors of the PSF fitting at the nucleus removal step. A cut across the PSF subtracted image and the aperture photometry profile is presented in Figs. 8 and 9.

The best-fit NEATM nucleus SED ($R = 2.34 \pm 0.14 \text{ km}$) was subtracted from the extracted comet Encke spectra and then scaled to match the MIPS coma photometry. First, we scaled the separate modules by area to the fiducial $4.5''$ aperture. Next, we scaled the spectra to match the spectra overlap regions. Finally, we integrated the spectrum under the MIPS $24 \mu\text{m}$ bandpass to determine the final scale factors (Table 7). The SL spectrum from the 2004 June 25 05:28 UT epoch was dominated by the errors after nucleus subtraction (i.e., the coma was at low signal to noise), hence the large scale factor of 1.53. The final, combined 2004 June 25 05:28 UT epoch spectrum is presented in Fig. 10.

We repeat this procedure for the 2004 June 25 08:27 UT epoch, high-resolution spectrum of Encke. The NEATM nucleus predicts a flux larger than observed in the SL spectrum data points by more than one standard deviation (overall, $\chi^2_\nu = 22$). An improperly centered

(within the slit) comet could cause such a photometric error, or the nucleus may be presenting a larger cross section to the telescope than the $R = 2.34$ km model provides. We cannot estimate the coma flux in this module and therefore drop SL from the analysis. The SH and LH scale factors (Table 7) account for the asymmetric dust morphology of comet Encke and the shape and orientation of the slits. The final spectrum is presented in Fig. 10.

The comet Encke spectra are modeled using a thermal grain model developed by Harker et al. (2002, 2006) which self-consistently calculates the temperature and thermal emission from a cometary dust mixture using laboratory optical constants. The minerals include amorphous carbon, amorphous pyroxene, amorphous olivine, and crystalline olivine. The amorphous carbon is used to represent warm, featureless continuum from deeply absorbing grains. The amorphous pyroxene and amorphous olivine grains are a 50-50 mixture of magnesium and iron which have an increased temperature as compared to pure-magnesium grains. The increased temperature was required to adequately model the silicate features in the thermal spectrum of comet Hale-Bopp (Harker 1999; Harker et al. 2002). The crystalline olivine grains are magnesium-pure (forsterite).

The thermal model invokes a Hanner grain size distribution (HGSD; Hanner 1983) to calculate the emission from a population of grains, $n(a)da$ with radii, a , varying from 0.1–100 μm . The grain population is described by a modified power law,

$$n(a) = \left(1 - \frac{a_0}{a}\right)^M \left(\frac{a_0}{a}\right)^N, \quad (3)$$

where a is the grain radius, a_0 is the minimum grain radius (assumed to be 0.1 μm), N is the slope of the distribution at large a , and M is related to the radius of the peak of the grain size distribution, a_p , by

$$a_p = a_0 \frac{M + N}{N}. \quad (4)$$

This choice of grain size distribution is known to reproduce the observed SEDs of many comets in the 3.5–20 μm wavelength range. Model grains can be fractally porous, with a density described by

$$\rho(a) = \rho_0 \left(\frac{a}{a_0}\right)^{D-3}, \quad (5)$$

where ρ_0 is the bulk density and D is the fractal dimension of the dust (solid spheres have D equal to 3, porous spheres have $D < 3$). To keep coma fitting tractable, we chose discrete values of a_p (0.1 μm steps) and D [one of 3.0, 2.857, 2.727, 2.609, and 2.5 (see Harker et al. 2002)], and all minerals in a given observation are assumed to have the same grain size distribution. After a best-fit model is derived, we attempt to estimate the error in peak grain size by exploring the curvature of χ^2 space with respect to a_p . For the Encke and

HT50 best-fits below, the derived a_p errors are $\lesssim 0.01 \mu\text{m}$. Given the small formal errors in a_p , our choice of $0.1 \mu\text{m}$ steps ensures our derived peak grain sizes are within $0.05 \mu\text{m}$ from the best values.

The coma of comet Encke was fitted ($\chi_\nu^2 = 0.5\text{--}0.9$) with a porous ($D = 2.857$), amorphous carbon mineralogy and a peak grain size of $0.4 \mu\text{m}$ ($N = 3.7$, $M = 11.1$). The model spectra (solid curve) are shown in Fig. 10. The agreement in best-fits between the low-resolution and high-resolution data suggest our reduction methods are consistent, regardless of the IRS module. The number of peak grains and upper-limits to olivine and pyroxene minerals are presented in Table 8. Our best-fit model constrains the sub-micron silicate fraction to $< 31\%$ by mass. The small peak grain size suggests that comet Encke has not exhausted its reservoir of small particles, but the large particle slope parameter, $N = 3.7$, does not preclude the importance of large particles. For our derived PSD, the ratio of the total mass of particles with $0.1 \mu\text{m} \leq a \leq 1 \mu\text{m}$ to the total mass of particles with $1 \mu\text{m} \leq a \leq 10 \mu\text{m}$ is 0.076, i.e., the sub-micron particles are a minor component of the total coma mass. Discussion of comet Encke’s mineralogy is presented in §4.2.

3.2. 67P/Churyumov-Gerasimenko

The peak up image of 67P (Fig. 5) showed a point source with a full-width at half-maximum of 3 pixels, or 18,000 km at the distance of the comet. Although the dust production of Jupiter-family comets at 5 AU is generally assumed to be minimal or non-existent, a point source does not indicate a bare nucleus. A point source could also be a combination of nucleus and 1) a coma from recent (hours to weeks) activity, 2) a coma of slowly moving micrometer sized or larger particles ejected this perihelion passage, or 3) very large particles ($\gtrsim 100 \mu\text{m}$) entrained in 67P’s debris trail. Assuming only a bare nucleus, we fitted the spectrum with the NEATM ($\eta = 0.756$, $p_v = 0.04$, and $\epsilon = 0.9$). The fit yielded a nucleus radius of $3.17 \pm 0.06 \text{ km}$ ($\chi_\nu^2 = 1.3$) and is presented along with the spectrum in Fig. 11.

Our derived best-fit effective radius for this comet is inconsistent with recent estimates of 67P’s nucleus size (Lamy et al. 2004). For example, Lamy et al. (2003) derive a value of $1.98 \pm 0.02 \text{ km}$ using the *Hubble Space Telescope*, and Kelley et al. (2005a) estimate a value of $1.91 \pm 0.09 \text{ km}$ using *Spitzer*/MIPS. It is clear our *Spitzer* spectrum of comet 67P is not that of a bare nucleus. Likely, some amount of dust still enshrouds the nucleus at 5 AU. The nucleus subtracted spectrum is not of high enough quality or spectral range for a detailed coma fit. When the Kelley et al. (2005a) NEATM fit, calculated for the epoch of the spectrum, is subtracted, the resulting spectrum constrains the dust contribution. The observed coma flux is $2.01 \pm 0.10 \times 10^{-21} \text{ W cm}^{-2} \mu\text{m}^{-1}$ at $27.9 \mu\text{m}$ (weighted average from

21–35 μm).

One component of 67P’s dust emission at this large heliocentric distance is the comet’s debris trail. To determine the fraction of the flux originating from the trail, we use the trail parameters determined by Sykes & Walker (1992) from *IRAS* measurements. In the *Spitzer* observations, the trail contributes $5.1 \pm 0.6 \times 10^{-23} \text{ W cm}^{-2} \mu\text{m}^{-1}$, or $2.5 \pm 0.3\%$, to the IRS spectrum. We can further refine this estimate by taking into account the effect of the orbital motion at 5 AU in an eccentric orbit. Here, particles in similar orbits will move slower, and hence be closer together, than at $r_h = 2.3 \text{ AU}$ (the epoch of the *IRAS* observations). To estimate the optical depth enhancement caused by this effect, we differentiate the true anomaly with respect to heliocentric distance

$$\frac{df}{dr} = \frac{-(1/e + \cos f)}{r \sin^2 f}, \quad (6)$$

where f is the true anomaly at the time of observation ($f = 96.9^\circ$ at the *IRAS* epoch, $f = 156.0^\circ$ at the *Spitzer* epoch) and $e = 0.632$ is the eccentricity of the orbit of comet 67P. The ratio of optical depths from the *IRAS* epoch to the *Spitzer* epoch is 1.25, increasing the trail contribution to 3%. The majority of the dust emission detected by *Spitzer* likely arises from 1) recently ejected dust (age of order hours to weeks), 2) large, slowly moving particles from the 2003 perihelion passage [evidenced by the shallow post-perihelion r_h dependence of dust from optical observations (Schleicher 2006)], or 3) some combination of the two.

The SED of 67P increases in flux density from 14–20 μm , then flattens (in slope) beyond 20 μm (Fig. 11). In principle, the color-temperature of the coma can constrain the mineral composition of the emitting dust. We attempted to account for the spectral shape by fitting the spectrum with our thermal model, constrained to one mineral (amorphous olivine or amorphous carbon) and constrained to specific peak grain sizes ($a_p = 1, 5, 15,$ or $30 \mu\text{m}$). For similarly sized particles, amorphous carbon dust has a higher color-temperature than amorphous olivine, and thus produces a poorer fit to the data. Also, smaller sized particles are warmer and produce poorer fits. The best-fit model consisted of large ($a_p \approx 15 \mu\text{m}$) amorphous olivine grains. For models of amorphous olivine dust, χ^2_ν ranged from 0.57 ($a_p = 15 \mu\text{m}$, maximum grain size of $30 \mu\text{m}$) to 0.73 ($a_p = 1 \mu\text{m}$, maximum grain size of $100 \mu\text{m}$). The increased maximum grain size in the $a_p = 1 \mu\text{m}$ model balances the warmer, $\approx 1 \mu\text{m}$ particles so that the resultant model spectrum fits the observed color-temperature. Overall, the low signal-to-noise ratio of the SED and the small range of grain temperatures for 1–100 μm grains at 5.0 AU ($T \approx 100\text{--}150 \text{ K}$) prohibits a detailed discussion of 67P’s dust coma mineralogy.

3.3. C/2001 HT50 (LINEAR-NEAT)

Inspection of the comet HT50 peak-up images (Fig. 5) reveals a bright coma at both epochs ($r_h = 3.2$ and 4.6 AU). We inspected the peak-up images for the signature of a point source. The peak-up image at $r_h = 3.2$ AU is saturated over the center five pixels and does not yield any information on the nucleus. The profile of the peak-up image at $r_h = 4.6$ AU does not exhibit a point source within the coma profile. We therefore proceed with the assumption that the nucleus contribution at each epoch is negligible and do not subtract a model nucleus from the HT50 spectra.

All IRS spectra were scaled to the nominal 4.5" aperture to mitigate module photometric mis-matches. Similar to the comet Encke spectra, the extracted HT50 spectra must be further scaled to account for varying slit orientations, coma asymmetries (Fig. 5), and the overall coma profile (Table 7). The spectra and our best-fit thermal models are presented in Figs. 12 and 13, and in Table 9.

The best-fit thermal models have a large peak grain size of 1.2 μm and a mixed amorphous carbon and silicate mineralogy ($N = 4.2$, $M = 46.2$, $\chi_\nu^2 = 4.2$ at 3.2 AU and $N = 3.7$, $M = 29.6$, $\chi_\nu^2 = 23.8$ at 4.6 AU). The total number of amorphous carbon grains from 0.1–10 μm varies from $\approx 5.8 \times 10^{19}$ ($r_h = 3.2$ AU) to $\approx 4.6 \times 10^{19}$ ($r_h = 4.6$ AU). A number of factors contribute to the number of observed grains, including the changing grain size distribution, the aperture size at the distance of the comet, the shape of the coma, and the dependence of coma activity on heliocentric distance (including phenomena such as jet activity and gas/dust outbursts). We cannot account for the heliocentric dependence of the dust production without a more rigorous temporal sampling of the coma at these epochs.

Our best-fit model indicates a weak detection of crystalline olivine in HT50 at 3.2 AU with a signal-to-noise ratio of 4. Figure 14 presents a closer analysis of the crystalline fit. Here, the spectrum was smoothed by a seven-point statistically weighted, moving average to increase the signal-to-noise of the spectrum. The spectrum was then normalized by the best-fit model, excluding the crystalline component. Excess emission (above unity in the normalized spectrum) is potentially due to crystalline olivine dust emission (represented in the figure by the solid line). The chi-squared fitting of the 1-sigma correlated errors indicates that a better fit ($\Delta\chi_\nu^2 = 0.04$) is obtained with crystalline olivine present rather than absent (to 4- σ or > 99% confidence). Inspection of Fig. 14 suggests the detection of crystals is driven by the shape of the spectrum at 22–24 μm . Altogether, the *Spitzer* observations suggest the presence of crystalline olivine in comet HT50. The mineralogy of comet HT50 is discussed and compared to other Oort cloud comets in §4.2.

4. DISCUSSION

4.1. The IR Beaming Parameter

Recent observations of near-Earth objects (NEO) suggest a possible dependence of η on phase angle (Delbó et al. 2003; Wolters et al. 2005). Delbó et al. derived an empirical η -phase angle correlation from observations of NEOs at phase angles $\phi \approx 5\text{--}60^\circ$. Wolters et al. added more data to the discussion and derived the trend $\eta = 0.69 + 0.012\phi$. However, extensive data to assess whether an η -phase angle correlation exists for *single* objects does not exist. Only one asteroid (2002 NY40) has been observed in detail at disparate phase angles and no η -phase dependence was found (Müller et al. 2004). Comet Encke is a near-Earth object, and observations of its nucleus can be used to assess the validity of the NEATM and the η -phase angle correlation.

To examine the potential correlation of the IR beaming parameter with phase angle, we will assume the nucleus has a radius equal to the radius derived from our 2004 June SED, $R = 2.34 \pm 0.14$ km. The IR beaming parameter is also best constrained by the 2004 June SED to a value of 0.735 ± 0.046 . With these parameters, the NEATM predicts a flux of 3.9 Jy for the (Fernández et al. 2000) observation on 1997 July 19 at a phase angle of 44° . However, Fernández et al. observed a flux density of 2.74 ± 0.24 Jy. The 2004 June derived radius and IR beaming parameter do not account for the observed flux in 1997 July, just as they did not account for the 2003 November SED (§3.1.1). The Fernández et al. 1997 July 8.5, 10.7, and 11.6 μm observations were fitted with the 2004 June radius and we derived a best-fit η value of 1.02 ± 0.11 . The 2003 November and 1997 July data sets are limited, but suggest a larger η value is required for higher phase angles.

An η -phase angle dependence can be a direct result of certain physical properties of the nucleus surface. There are two possible mechanisms that may produce the a change of η with phase angle (see Delbó et al. 2003; Wolters et al. 2005). Either, the surface roughness of the nucleus is exacerbated at high phase angles (i.e., the observer views an increasing amount of shadowing), requiring a lower temperature to model the nucleus; or alternatively, the night hemisphere of the nucleus does not completely cool to the background temperature and contributes appreciable flux at high phase angles, requiring a lower temperature to model the nucleus. We consider these possibilities in order.

In the former case, surface roughness causes severe shadowing across the diurnal hemisphere. At high phase angles, an observer could be viewing the shadowed side of a scarp or other surface topology as observed on the surfaces of comets 1P/Halley, Tempel 1, 19P/Borrelly, and 81P/Wild 2 (Keller et al. 1986; A’Hearn et al. 2005; Soderblom et al. 2002; Brownlee et al. 2004). This geometry presents an overall cooler surface when com-

pared to a smooth sphere at the same phase angle (see Delbó & Harris 2002, Fig. 5). This requires a lower temperature in the NEATM and, therefore, a higher IR beaming parameter. At low phase angles the contrary is true and an observer may be viewing more surfaces normal to the sun direction, thus requiring a hotter surface and lower IR beaming parameter in the NEATM, consistent with the Wolters et al. (2005) trend. The temperature map of the Tempel 1 nucleus by A’Hearn et al. (2005) clearly shows how local surface temperature relies on the topology of the nucleus. Surface roughness on smaller scales (e.g., in the regolith of small bodies) is also important in thermal observations (Shkuratov et al. 2000; Lagerros 1998) and necessary to explain polarization measurements of atmosphereless bodies (Petrova et al. 2001).

If surface elements on the night hemisphere contribute significant flux to an observer, they can lower the observed color-temperature. In the formalism of the NEATM, all radiation is assumed to arise from the sun-lit hemisphere and therefore a lower observed color-temperature will raise the derived η value. The temperature of the night hemisphere will depend upon the angular rotation rate of the nucleus and the ability of the surface to hold heat, i.e., its thermal inertia. Following Spencer et al. (1989) and Fernández et al. (2000) we can test whether or not the Encke nucleus could be considered a fast or slow rotator. A slow rotator model uses the same assumptions as the STM and NEATM, i.e., the sub-solar point is the hottest point and the night side emits no light. A fast rotator model assumes the cooling time scale is longer than the rotation period and, therefore, the object will be isothermal with respect to latitude. The unit less parameter Θ is used to determine the applicability of the two models,

$$\Theta = \frac{\Gamma\sqrt{\omega}}{\epsilon\sigma T_{ss}^3}, \quad (7)$$

where Γ is the thermal inertia in $\text{J K}^{-1} \text{m}^{-2} \text{s}^{-1/2}$ and ω is the angular rotation rate of the object in s^{-1} . Slow rotators have $\Theta \ll 1$ and fast rotators have $\Theta \gg 1$. We chose 10 and $320 \text{ J K}^{-1} \text{m}^{-2} \text{s}^{-1/2}$ as the thermal inertia extrema for short period comets, as suggested by the observations of the sub-solar temperature of Tempel 1 (A’Hearn et al. 2005) and ground-based observations of (3200) Phaethon (Green et al. 1985). Fernández et al. (2005) derived two possible periods for the Encke nucleus, 11.1 or 22.2 hr. The 11.1 hr rotation period has been verified by radar observations (Harmon & Nolan 2005). To determine the sub-solar temperature we use our best NEATM fits, $\eta = 1.026$ at 1.1 AU and $\eta = 0.735$ at 2.6 AU, which produces $T_{ss} = 382 \text{ K}$ at 1.1 AU and 269 K at 2.6 AU. Together, Θ ranges 0.02–0.6 at 1.1 AU and 0.05–1.6 at 2.6 AU. With these new measurements we conclude, as did (Fernández et al. 2005), that at best we can use a slow rotator model (if $\Gamma \approx 10 \text{ J K}^{-1} \text{m}^{-2} \text{s}^{-1/2}$) and at worst the Encke nucleus is in an intermediate state between slow and fast rotation (if $\Gamma \approx 320 \text{ J K}^{-1} \text{m}^{-2} \text{s}^{-1/2}$). Additionally, there is no clear transition to a fast rotator as

Encke recedes from the sun.

We also note the recent mid-infrared measurements of asteroid 2002 NY40 by Müller et al. (2004) at phase angles of 22° and 59° show no η -phase angle dependence. Although the majority of the observations suggest the dependence (Wolters et al. 2005), the relation may not hold true for any particular object. The case of comet Encke is not resolved. The observed SEDs are fit by an η parameter that varies with phase angle but may also be fit by changing the observed effective radius within the constraints of the derived nucleus shape. An SED of the Encke nucleus at high phase angle that constrains both effective radius and color temperature is required to support either possibility.

4.2. Comet Mineralogy

The mineralogies of comet HT50’s dust coma at both epochs are consistent with each other given the errors and upper-limits (Table 10). Also presented in Table 10 are the mineralogies of comets Hale-Bopp and Tempel 1, pre- and post-*Deep Impact* encounter (Harker et al. 2004, 2005). The low mass ratio between the silicate minerals and the deeply absorbing grains (represented by amorphous carbon) appears to be intermediate between the aging Jupiter-family comet Encke and the presumably pristine materials ejected from comet Hale-Bopp and comet Tempel 1 (post-*Deep Impact*). Does comet HT50 have a processed surface similar to what may be on the surfaces of Jupiter-family comets? Even comet C/2001 Q4 (NEAT) exhibited a large range in silicate-to-carbon ratios, varying from 2.7–5.7 in ≈ 1 hour (Wooden et al. 2004). Comet Q4, like Hale-Bopp, showed strong jets (Lecacheux & Frappa 2004) and Q4’s high silicate fractions may originate in the (local) jet activity. In comet jets, violent sublimation of ices and volatile gases may excavate and entrain pristine grain materials from sub-surface reservoirs within the nucleus, similar to the *Deep Impact* event. Visual inspection of the *Spitzer* images of HT50 (Fig. 5) show no distinct jet-features in the coma and there were no reports of any outbursts by this comet. Therefore, it may be that comet HT50 is dominated by “whole surface” (global) sublimation and that Jupiter-family and long period/Oort cloud comets are somewhat similar in the structure of their immediate surfaces. Indeed, it has been proposed that Oort cloud comets can form a cohesive crust from normal re-surfacing processes, including galactic cosmic rays (Strazzulla & Johnson 1991), supernovae (Stern & Shull 1988), and interstellar grain impacts (Stern 1986). It is apparent that more work determining the mineralogy of comet comae is needed to understand the extent of the silicate-to-carbon ratio variations in comets, its correlation with nucleus activity, and possible connections to nucleus surface structure.

Previous narrow-band photometry of comet Encke indicated a weak silicate feature at

small heliocentric distances (Campins et al. 1982; Gehrz et al. 1989) but no feature at 1.2 AU (Lisse et al. 2004). The coma is usually considered to be dominated by large particles, based upon a low coma color-temperature and a lack of a strong silicate feature (Gehrz et al. 1989; Reach et al. 2000; Lisse et al. 2004). Instead, our best-fit models indicate silicates are a minor constituent ($< 31\%$ by mass for $a \leq 1 \mu\text{m}$) to the coma. To compare our results to previous investigations near perihelion, we computed a “silicate upper-limit” model derived from our best-fit Encke mineralogy in Table 8. The upper-limit model sets the number of peak grains for the silicate minerals to their three-sigma upper-limits and decreases N_p for the amorphous carbon component by three-sigma. The mineral ratio by sub-micron mass becomes 100:1:18:11 (amorphous carbon:amorphous olivine:amorphous pyroxene:crystalline olivine). The upper-limit model and photometry of comet Encke at perihelion in 1987 July from Gehrz et al. (1989) is presented in Fig. 15. Also included is the Encke nucleus as derived from Table 6 ($R = 2.34 \text{ km}$, $\phi = 63^\circ$). The coma and nucleus models were computed for the same geometry as the photometry data ($r_h = 0.38 \text{ AU}$, $\Delta = 1.13 \text{ AU}$, $\phi = 63^\circ$). The coma model was scaled to account for Encke’s difference in dust production between $r_h = 0.38 \text{ AU}$ and 2.4 AU .

The upper-limit model produces a silicate feature at $10 \mu\text{m}$ that approximates the weak silicate excess exhibited by the $9\text{--}13 \mu\text{m}$ photometry points. The general shape of the SED is also approximated by the model, except for the short wavelength flux points, which are underestimated by factors of $1.2\text{--}1.8$. The model likely requires a contribution from scattered sunlight to account for the $2.2 \mu\text{m}$ and $3.6 \mu\text{m}$ data points. Only the $5 \mu\text{m}$ data point remains unexplained (the error bar may not reflect variations in atmospheric transparency through the optically thick $5 \mu\text{m}$ band-pass). Modifying the relative contributions of the silicates and carbonaceous minerals does not produce a satisfactory fit, although the possibility remains that the PSD could be varied to account for the spectral shape. We conclude that our *Spitzer*-derived mineralogy is a robust estimate of 2P/Encke’s coma composition and that our best-fit model’s PSD, derived at $r_h = 2.4 \text{ AU}$, may not be representative of the PSD observed throughout Encke’s entire orbit. Indeed, the brightness behavior near perihelion is asymmetric and is best explained by different active regions on the nucleus, therefore, a varying PSD about perihelion could be expected (Sekanina 1991).

Jupiter-family comets are thought to form in the transneptunian region and beyond (Duncan et al. 2004; Morbidelli & Brown 2004). We have derived mineralogies for two Jupiter-family comets: comet Encke, likely dominated by deeply absorbing grains, and comet Tempel 1 dominated by silicate grains (Harker et al. 2006). These are striking differences for two comets assumed to arise from the same region of the proto-solar disk. The difference in mineralogy may be due to each comet’s original compositions or may be a reflection of different compositional processing histories. Ultraviolet and ion radiation transforms

relatively optically inactive organic material into a dark, carbonized solid (Jenniskens et al. 1993; Greenberg et al. 1995). Outgasing from surfaces or sub-surface layers with different radiation exposures may explain the differences in the coma mineralogy of comets Encke and Tempel 1. Alternatively, the outgasing surfaces or sub-surface layers may have original and different compositions. Such layering in Jupiter-family comet nuclei has been proposed by Belton & Deep Impact Science Team (2006) to account for topographical features on comets Tempel 1, Borrelly, and Wild 2.

5. CONCLUSIONS

We present *Spitzer*/IRS spectra of comets 2P/Encke, 67P/Churyumov-Gerasimenko, and C/2001 HT50 (LINEAR-NEAT), and *Spitzer*/IRAC and MIPS images of comet 2P/Encke. Comet Encke exhibited a smooth continuum, best modeled by carbonaceous grains with a small peak grain size ($a_p = 0.4 \mu\text{m}$). Previous investigations into comet Encke’s dust coma revealed a weak silicate feature at perihelion ($r_h = 0.3 \text{ AU}$). We conclude the weak silicate feature is due to the paucity of silicate grains and the preponderance of carbonaceous grains (or some other warm, deeply absorbing material). We constrain the sub-micron silicate fraction to $< 31\%$ by mass. The nucleus of comet Encke is fit by the near-Earth asteroid thermal model with an effective radius $R = 2.34 \pm 0.14$. The nucleus was observed at phase angles 20° and 63° and may be exhibiting a variation of the infrared beaming parameter with phase angle, which indicates of a rough nucleus surface or appreciable night side temperature.

Comet 67P exhibited a significant coma at a heliocentric distance of 5 AU, $F_\lambda = 2.01 \pm 0.10 \times 10^{-21} \text{ W cm}^{-2} \mu\text{m}^{-1}$ at $27.9 \mu\text{m}$. 67P’s known dust trail comprises approximately 3% of the measured dust flux density. The remaining coma flux was due to 1) recently ejected dust (age of order hours to weeks), 2) large, slowly moving particles from the 2003 perihelion passage, or 3) some combination of the two.

Comet HT50 displayed a significant silicate mineralogy with a silicate-to-carbon sub-micron mass ratio of 0.6. The derived ratio of 0.6 is an order of magnitude lower than the silicate-to-carbon ratios of post-*Deep Impact* comet 9P/Tempel 1 and other Oort cloud comets, C/1995 O1 (Hale-Bopp) and C/2001 Q4 (NEAT).

The differences in silicate-to-carbon mass ratios in comet comae may be linked to strong jet activity in comets. Comet HT50’s derived silicate-to-carbon sub-micron mass ratio is 0.6, but analysis of comet Hale-Bopp, which exhibited strong jet activity, derived a ratio of 8.1. At this time, the wide diversity in comet comae mineralogy likely has not been probed.

The authors thank William Reach for useful discussions and comments. In addition, the authors wish to thank the referee for their insightful comments and suggestions that improved the manuscript. This work is based on observations made with the Spitzer Space Telescope, which is operated by the Jet Propulsion Laboratory, California Institute of Technology under a contract with NASA. Support for this work was provided by NASA through contracts 1256406, 1263741, 1275835, issued by JPL/Caltech to the University of Minnesota. C.E.W. and M.S.K. acknowledge support from the National Science Foundation grant AST-037446. M.S.K. acknowledges support from the University of Minnesota Doctoral Dissertation Fellowship.

Facilities: Spitzer

REFERENCES

- A’Hearn, M. F. 2004, *Comets II*, 17
- A’Hearn, M. F., et al. 2005, *Science*, 310, 258
- Belton, M. J. S., & Deep Impact Science Team 2006, 37th Annual Lunar and Planetary Science Conference, 37, 1232
- Brownlee, D. E., et al. 2004, *Science*, 304, 1764
- Campins, H. 1988, *Icarus*, 73, 508
- Campins, H., A’Hearn, M. F., & McFadden, L.-A. 1987, *ApJ*, 316, 847
- Campins, H., Rieke, G. H., & Lebofsky, M. J. 1982, *Icarus*, 51, 461
- Delbó, M., & Harris, A. W. 2002, *Meteoritics and Planetary Science*, 37, 1929
- Delbó, M., Harris, A. W., Binzel, R. P., Pravec, P., & Davies, J. K. 2003, *Icarus*, 166, 116
- Dones, L., Weissman, P. R., Levison, H. F., & Duncan, M. J. 2004, *Comets II*, 153
- Duncan, M., Levison, H., & Dones, L. 2004, *Comets II*, 193
- Ehrenfreund, P., Charnley, S. B., & Wooden, D. 2004, *Comets II*, 115
- Fazio, G. G., et al. 2004, *ApJS*, 154, 10
- Fernandez, Y. R. 1999, Ph.D. Thesis (University of Maryland, College Park)

- Fernández, Y. R., Lowry, S. C., Weissman, P. R., Mueller, B. E. A., Samarasinha, N. H., Belton, M. J. S., & Meech, K. J. 2005, *Icarus*, 175, 194
- Fernández, Y. R., et al. 2000, *Icarus*, 147, 145
- Gehrz, R. D., Ney, E. P., Piscitelli, J., Rosenthal, E., & Tokunaga, A. T. 1989, *Icarus*, 80, 280
- Gehrz, R. D., Reach, W. T., Woodward, C. E., & Kelley, M. S. 2006, *Adv. Space Res.*, in press
- Green, S. F., Meadows, A. J., & Davies, J. K. 1985, *MNRAS*, 214, 29P
- Greenberg, J. M., Li, A., Mendoza-Gomez, C. X., Schutte, W. A., Gerakines, P. A., & de Groot, M. 1995, *ApJ*, 455, L177
- Hanner, M. S. 1983, *Cometary exploration; Proceedings of the International Conference, Budapest, Hungary, November 15-19, 1982. Volume 2 (A84-47701 23-90)*. Budapest, Akademiai Kiado, 1983, p. 1-22. *NASA-supported research.*, 2, 1
- Hanner, M. S., Giese, R. H., Weiss, K., & Zerull, R. 1981, *A&A*, 104, 42
- Hanner, M. S., Lynch, D. K., Russell, R. W., Hackwell, J. A., Kellogg, R., & Blaney, D. 1996, *Icarus*, 124, 344
- Harker, D. E. 1999, Ph.D. Thesis (Univ. Wyoming)
- Harker, D. E., Wooden, D. H., Woodward, C. E., & Lisse, C. M. 2002, *ApJ*, 580, 579
- Harker, D. E., Wooden, D. H., Woodward, C. E., & Lisse, C. M. 2004, *ApJ*, 615, 1081
- Harker, D. E., Woodward, C. E., & Wooden, D. H. 2005, *Science*, 310, 278
- Harker, D. E., Woodward, C. E., Wooden, D. H., Fisher, S., & Trujillo, C. 2006, *Icarus*, submitted
- Harker, D. E., Woodward, C. E., Wooden, D. H., Witteborn, F. C., & Meyer, A. W. 1999, *AJ*, 118, 1423
- Harmon, J. K., & Nolan, M. C. 2005, *Icarus*, 176, 175
- Harris, A. W. 1998, *Icarus*, 131, 291
- Honda, M., et al. 2004, *ApJ*, 601, 577

- Houck, J. R., et al. 2004, *ApJS*, 154, 18
- Jenniskens, P., Baratta, G. A., Kouchi, A., de Groot, M. S., Greenberg, J. M., & Strazzulla, G. 1993, *A&A*, 273, 583
- Jewitt, D. 1991, *ASSL Vol. 167: IAU Colloq. 116: Comets in the post-Halley era*, 19
- Keller, H. U., et al. 1986, *Nature*, 321, 320
- Kelley, M. S., Reach, W. T., & Lien, D. J. 2005a, *Icarus*, submitted
- Kelley, M. S., et al. 2005b, *American Astronomical Society Meeting Abstracts*, 206, 34.03
- Lagerros, J. S. V. 1998, *A&A*, 332, 1123
- Lamy, P. L., Toth, I., Fernandez, Y. R., & Weaver, H. A. 2004, *Comets II*, 223
- Lamy, P. L., Toth, I., Weaver, H., Jorda, L., & Kaasalainen, M. 2003, *AAS/Division for Planetary Sciences Meeting Abstracts*, 35, 30.04
- Lebofsky, L. A., et al. 1986, *Icarus*, 68, 239
- Lecacheux, J., & Frappa, E. 2004, *IAU Circ.*, 8349, 1
- Lisse, C. M., et al. 2004, *Icarus*, 171, 444
- Lisse, C. M., et al. 2005, *ApJ*, 625, L139
- Lynch, D. K., Russell, R. W., & Sitko, M. L. 2000, *Icarus*, 144, 187
- Lynch, D. K., Russell, R. W., & Sitko, M. L. 2002, *Icarus*, 159, 234
- Makovoz, D., Khan, I. 2005. Mosaicking with MOPEX. *Astronomical Society of the Pacific Conference Series* 347, 81.
- Morbidelli, A., & Brown, M. E. 2004, *Comets II*, 175
- Müller, T. G., Sterzik, M. F., Schütz, O., Pravec, P., & Siebenmorgen, R. 2004, *A&A*, 424, 1075
- Petrova, E. V., Jockers, K., & Kiselev, N. N. 2001, *Solar System Research*, 35, 390
- Pravdo, S., Helin, E., Lawrence, K., & Spahr, T. B. 2001, *IAU Circ.*, 7624, 1
- Reach, W. T., Sykes, M. V., Lien, D., & Davies, J. K. 2000, *Icarus*, 148, 80

- Reach, W. T., et al. 2005, *PASP*, 117, 978
- Rieke, G. H., et al. 2004, *ApJS*, 154, 25
- Schleicher, D. G. 2006, *Icarus*, 181, 442
- Sekanina, Z. 1991, *JRASC*, 85, 324
- Shkuratov, Y., Stankevich, D., Sitko, M. L., & Sprague, A. L. 2000, *ASP Conf. Ser.* 196: Thermal Emission Spectroscopy and Analysis of Dust, Disks, and Regoliths, 196, 221
- Sitko, M. L., Lynch, D. K., Russell, R. W., & Hanner, M. S. 2004, *ApJ*, 612, 576
- Soderblom, L. A., et al. 2002, *Science*, 296, 1087
- Spencer, J. R., Lebofsky, L. A., & Sykes, M. V. 1989, *Icarus*, 78, 337
- Spitzer Science Center. 2005, *Spitzer Observers' Manual* (Pasadena: SSC), <http://ssc.spitzer.caltech.edu/documents/som/>
- Spitzer Science Center. 2006a, *Infrared Array Camera Data Handbook* (Pasadena: SSC), <http://ssc.spitzer.caltech.edu/irac/dh/>
- Spitzer Science Center. 2006b, *Multiband Imaging Photometer for Spitzer (MIPS) Data Handbook* (Pasadena: SSC), <http://ssc.spitzer.caltech.edu/mips/dh/>
- Stansberry, J. A., et al. 2004, *ApJS*, 154, 463
- Strazzulla, G., & Johnson, R. E. 1991, *ASSL Vol. 167: IAU Colloq. 116: Comets in the post-Halley era*, 243
- Stern, S. A. 1986, *Icarus*, 68, 276
- Stern, S. A. 2003, *Nature*, 424, 639
- Stern, S. A., & Shull, J. M. 1988, *Nature*, 332, 407
- Sykes, M. V., & Walker, R. G. 1992, *Icarus*, 95, 180
- Veeder, G. J., Hanner, M. S., & Tholen, D. J. 1987, *AJ*, 94, 169
- Werner, M. W., et al. 2004, *ApJS*, 154, 1
- Whipple, F. L., & Hamid, S. E.-D. 1950, *AJ*, 55, 185
- Wolters, S. D., Green, S. F., McBride, N., & Davies, J. K. 2005, *Icarus*, 175, 92

Wooden, D. H., Harker, D. E., & Brearley, A. J. 2005, ASP Conf. Ser. 341: Chondrites and the Protoplanetary Disk, 341, 774

Wooden, D. H., Woodward, C. E., & Harker, D. E. 2004, ApJ, 612, L77

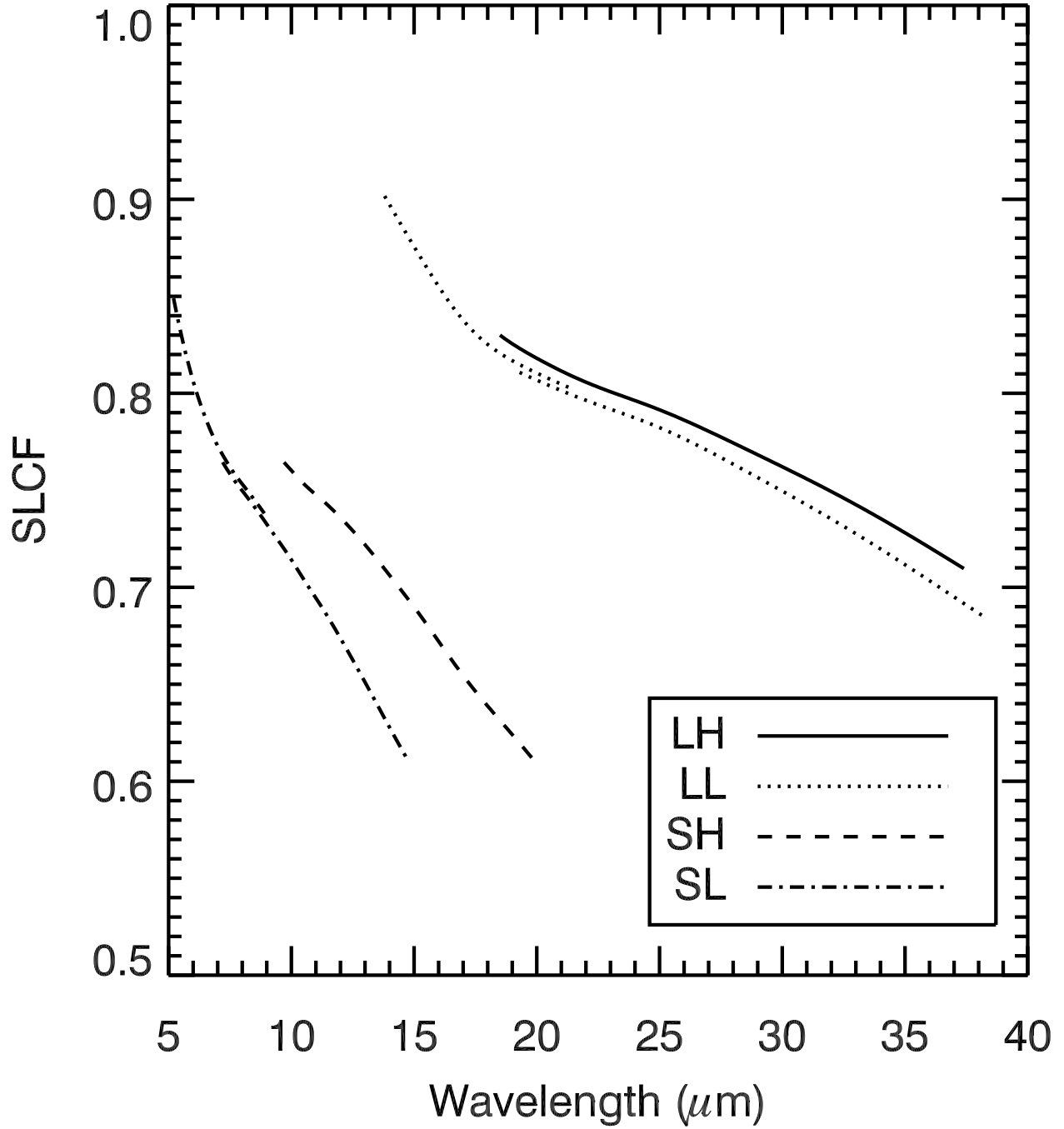


Fig. 1.— Slit loss correction factor for all IRS modules (see §2.1 for a discussion).

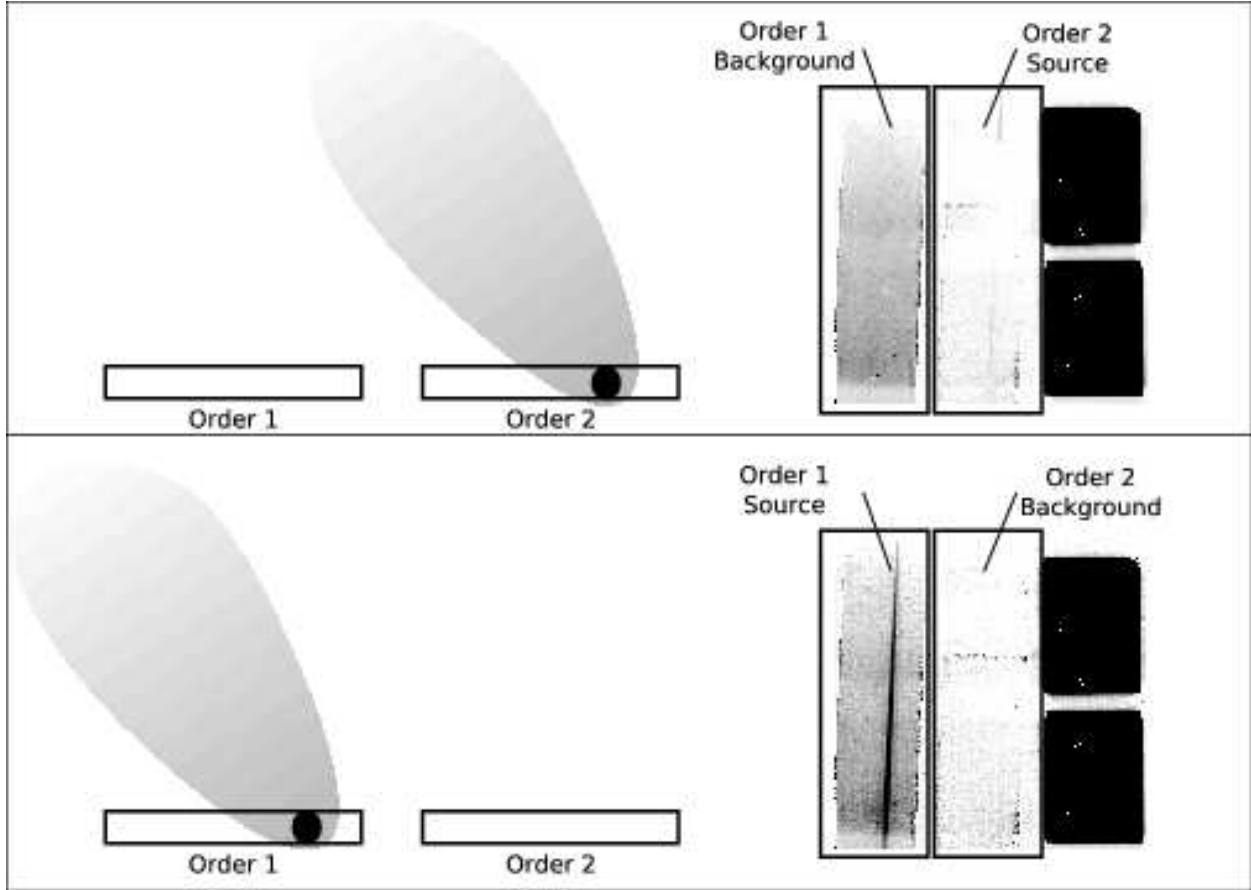


Fig. 2.— Schematic illustrating how background is removed in *Spitzer*/IRS low-resolution observations of extended sources. When the IRS observes the science target in one order (upper panel), the accompanying order provides a measurement of the background (lower panel). This strategy allows the background for a particular order to be two-dimensionally subtracted from the science observation.

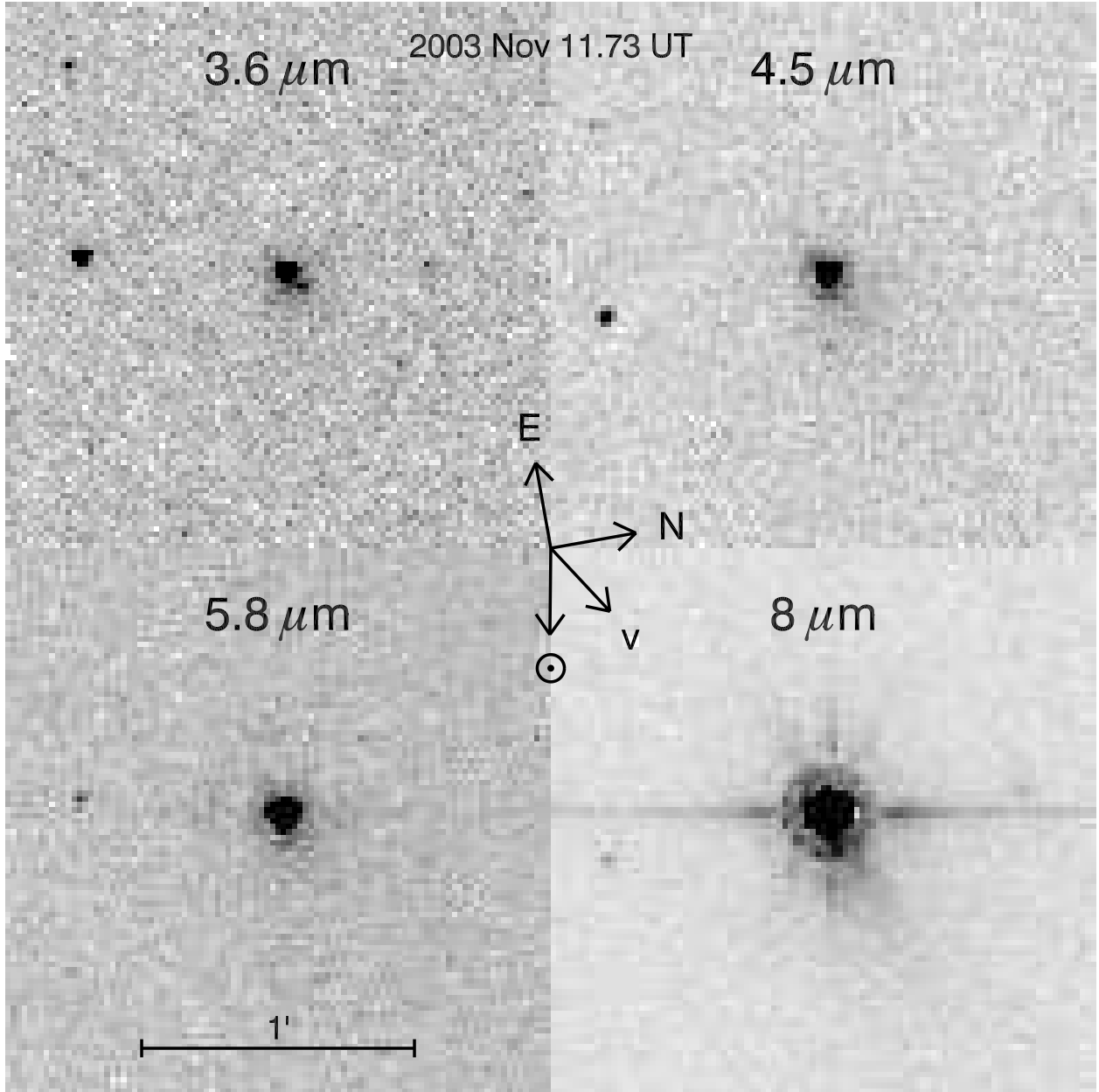


Fig. 3.— IRAC images of comet 2P/Encke obtained on 2003 Nov 11.73 UT. Each image displays a $2' \times 2'$ area centered on the comet with linear intensity scale. Arrows mark the image orientation (N, E), the projected velocity vector (v), and sun direction (\odot) as seen by *Spitzer*. The $8 \mu\text{m}$ image saturated on the nucleus.

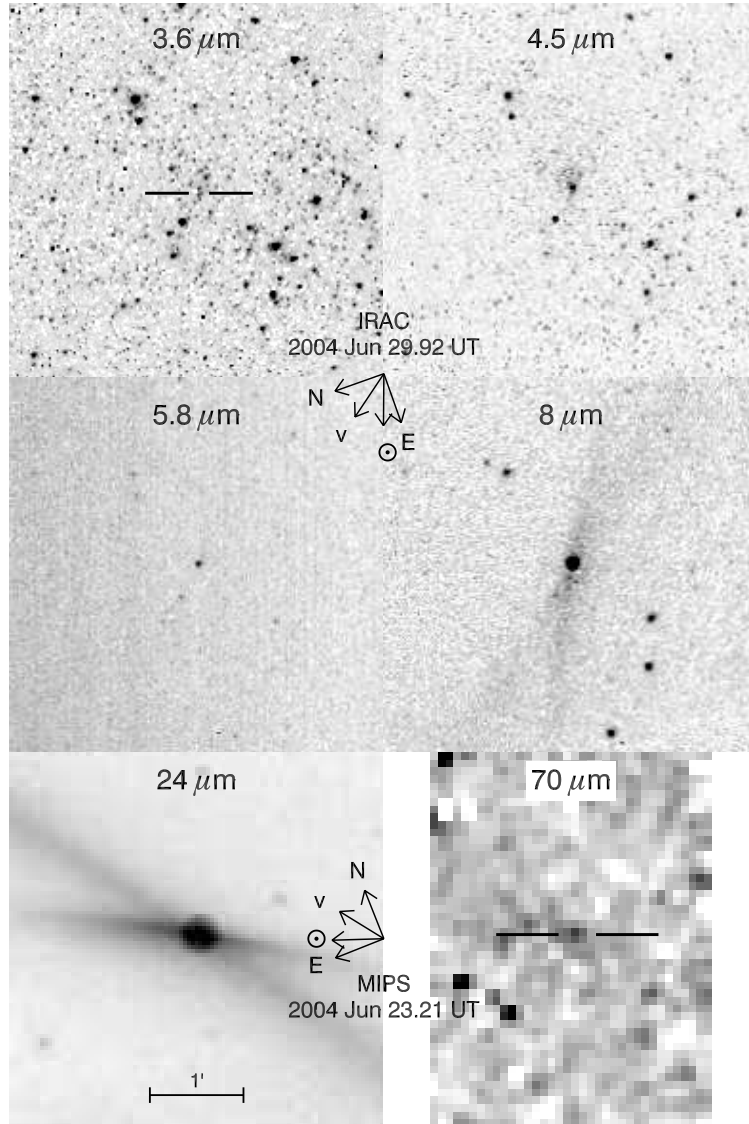


Fig. 4.— IRAC and MIPS mosaics of comet 2P/Encke obtained in 2004 June. Each image displays a $4' \times 4'$ area centered on the comet with a linear intensity scale. When the comet position is unclear, horizontal lines mark the location of the nucleus. The arrows are the same as in Fig. 3. The 3.6 to 8 μm orientations are labeled by the top set of arrows, and the 24 and 70 μm orientations are labeled by the bottom set of arrows. The near horizontal “spikes” in the 24 μm image are from recent comet activity and the emission stretching diagonally across the image is the dust trail (Gehrz et al. 2006).

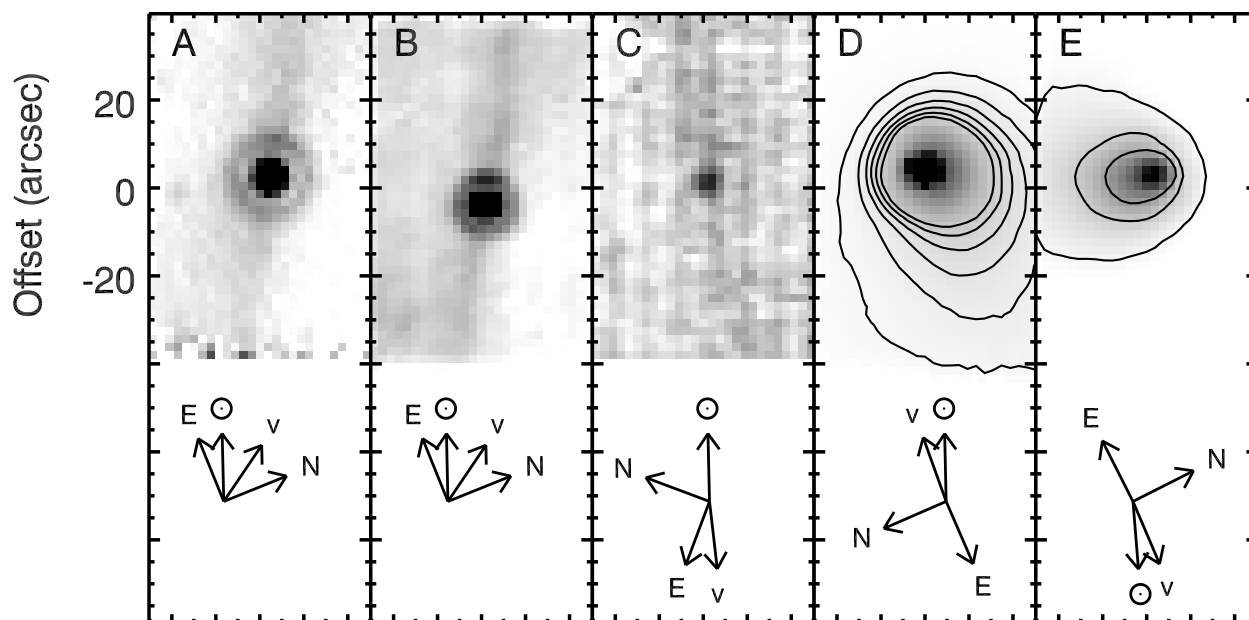


Fig. 5.— IRS peak up images and orientations for all comets. All images are co-added standard S12 pipeline BCDs using the red peak-up filter, unless noted: A) comet 2P/Encke, B) comet 2P/Encke, blue peak-up filter, C) comet 67P/Churyumov-Gerasimenko, SL flat-field applied, D) comet C/2001 HT50 (LINEAR-NEAT) at 3.2 AU with contours spaced every +2000 DN starting with 10000 DN and E) comet C/2001 HT50 (LINEAR-NEAT) at 4.6 AU with contours spaced every +2000 DN starting with 8500 DN. The comet 2P/Encke peak-ups also show the “spike” features evident in the MIPS image of Fig. 4.

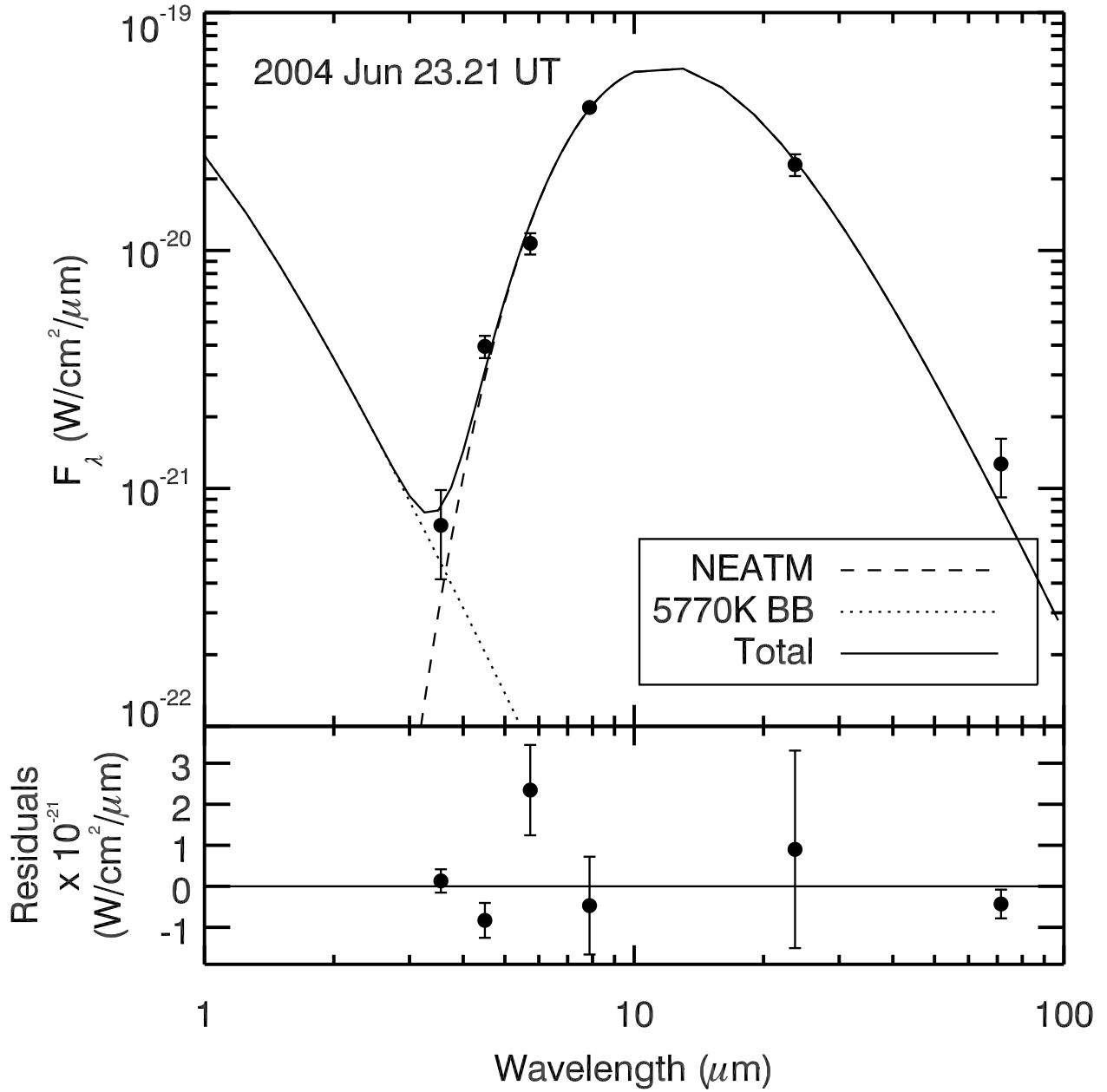


Fig. 6.— NEATM fit to comet 2P/Encke's nucleus and residuals for the 2004 June epoch.

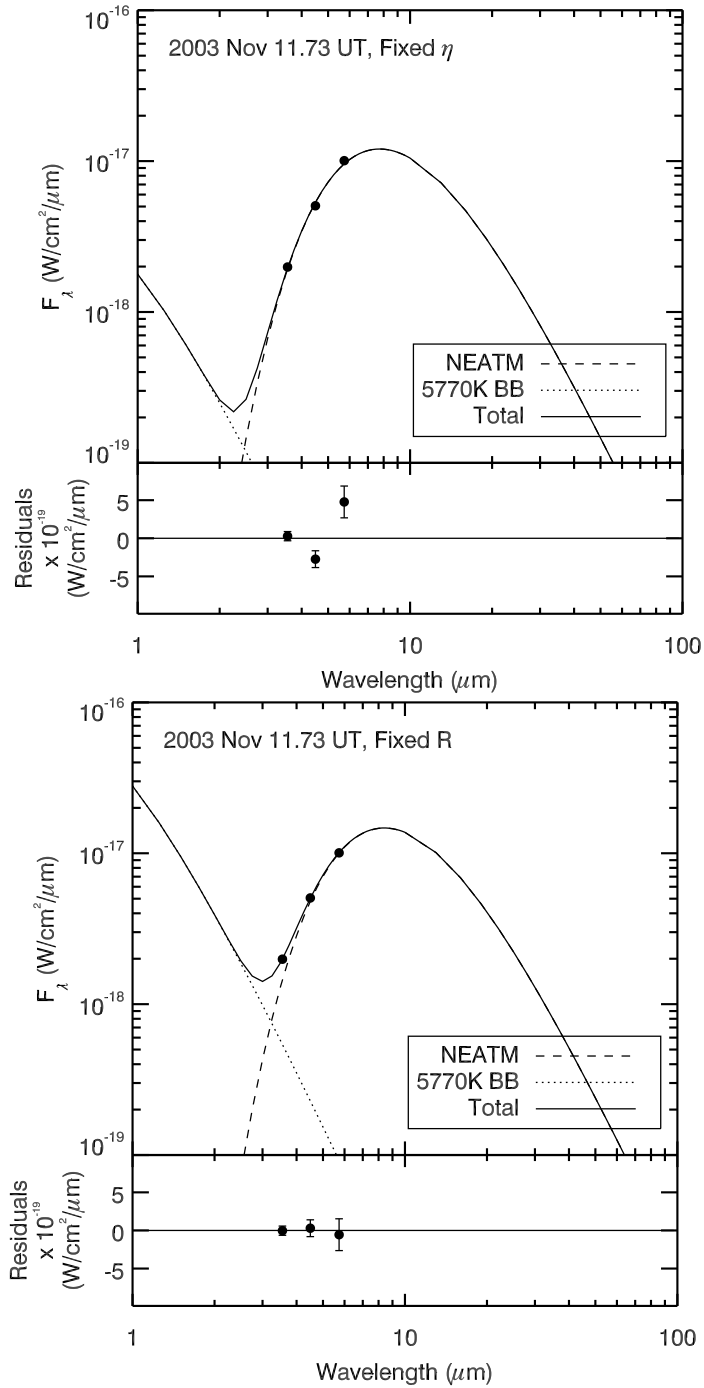


Fig. 7.— NEATM fits to comet 2P/Encke’s nucleus for the 2003 November epoch and their residuals. The fits correspond to the fixed η and fixed R fits in Table 6.

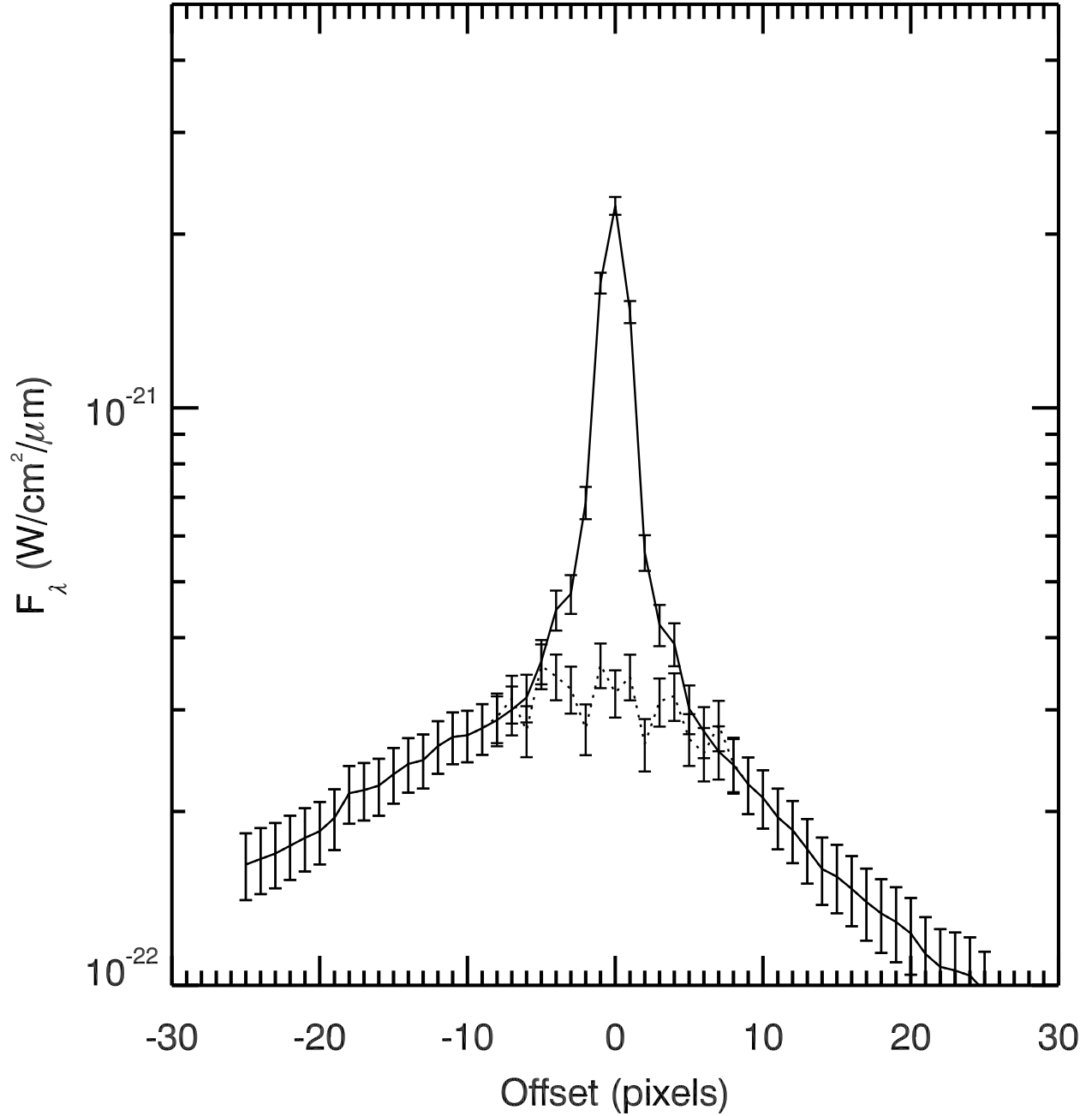


Fig. 8.— Cuts along the spike features and the nucleus in the MIPS image of comet 2P/Encke (position angle $\approx 81^\circ$; see Fig. 4). The solid-line is extracted from the original image, the dotted-line is extracted from the point source subtracted image.

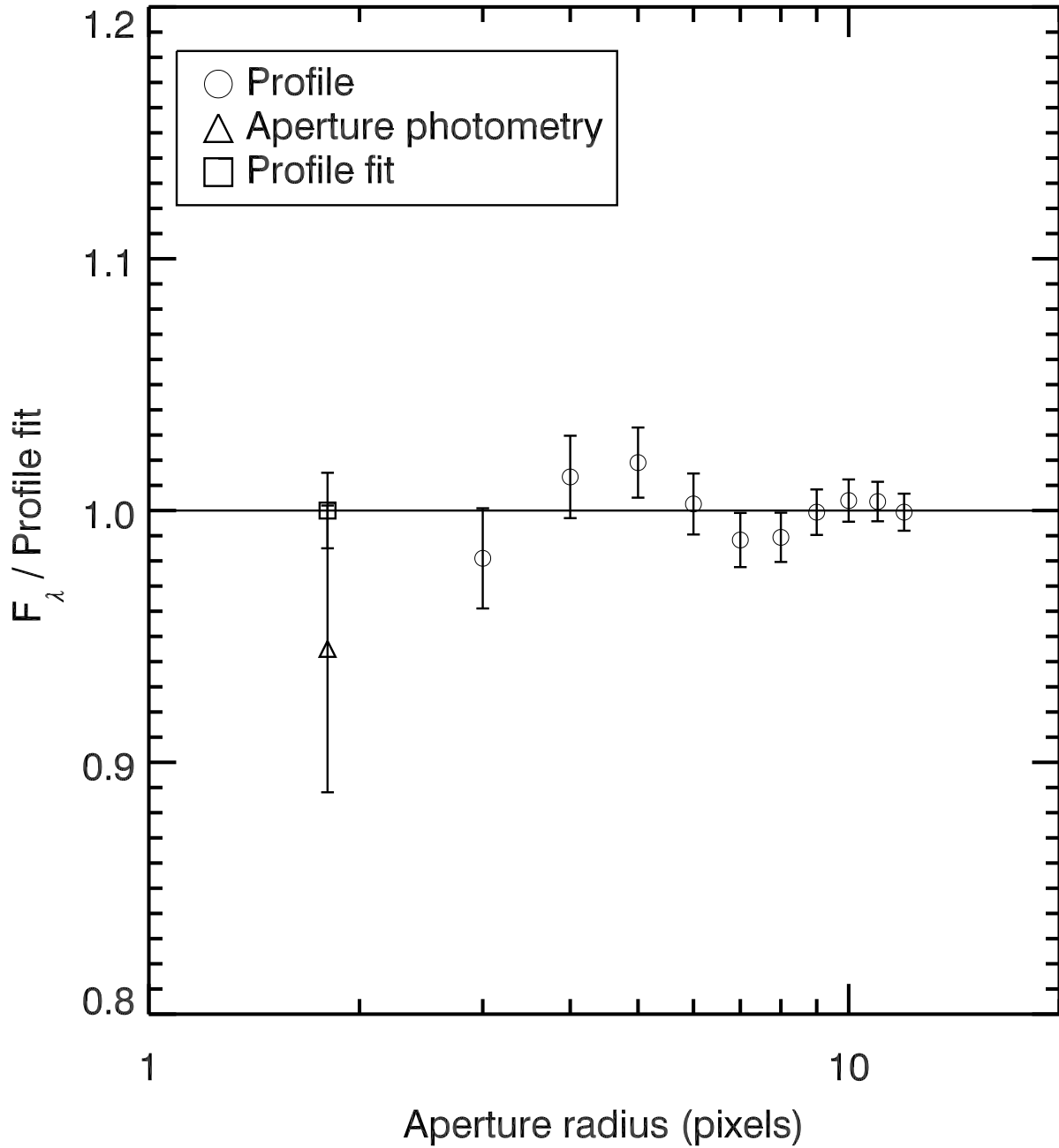


Fig. 9.— Azimuthally averaged aperture profile centered on the nucleus of comet 2P/Encke and normalized to the profile fit. The data points at 1.8 pixels (4.5") represent the coma fluxes in that aperture as determined by aperture photometry and profile fitting. The error on the profile fit at 1.8 pixels (\square) does not yet include the nucleus subtraction error.

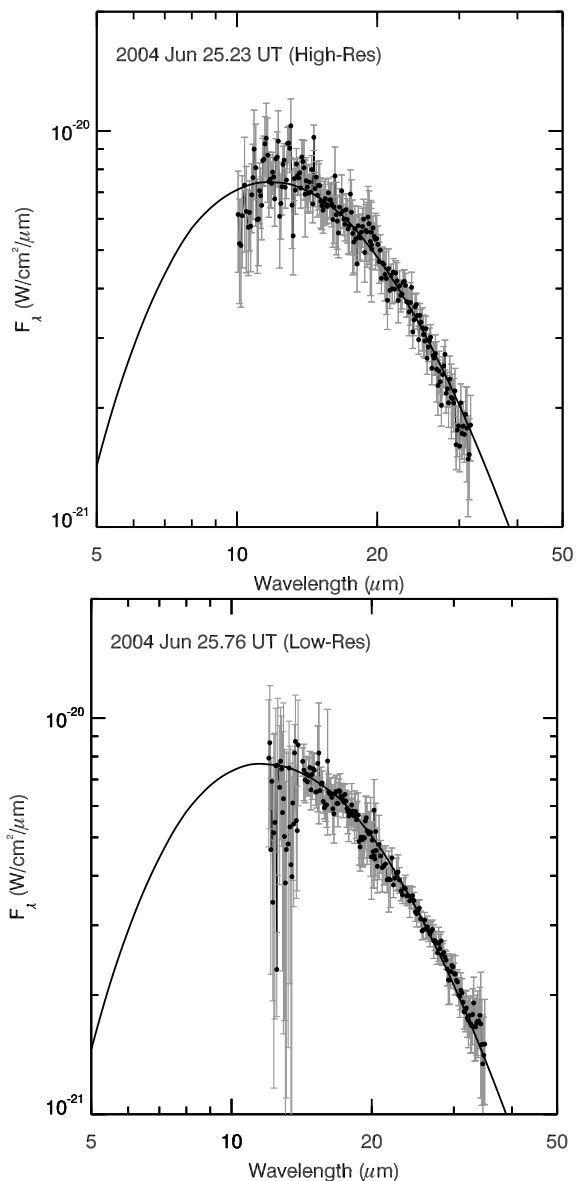


Fig. 10.— High-resolution and low-resolution IRS spectra of comet 2P/Encke. The high-resolution spectrum was degraded from $R \approx 600$ to $R \approx 85$ by a 7-point statistically weighted average. Both spectra were scaled to match the $24 \mu\text{m}$ coma photometry for a $4.5''$ radius aperture. The best-fit thermal emission models are shown as a solid-line ($N = 3.7$, $M = 11.1$, $a_p = 0.4 \mu\text{m}$).

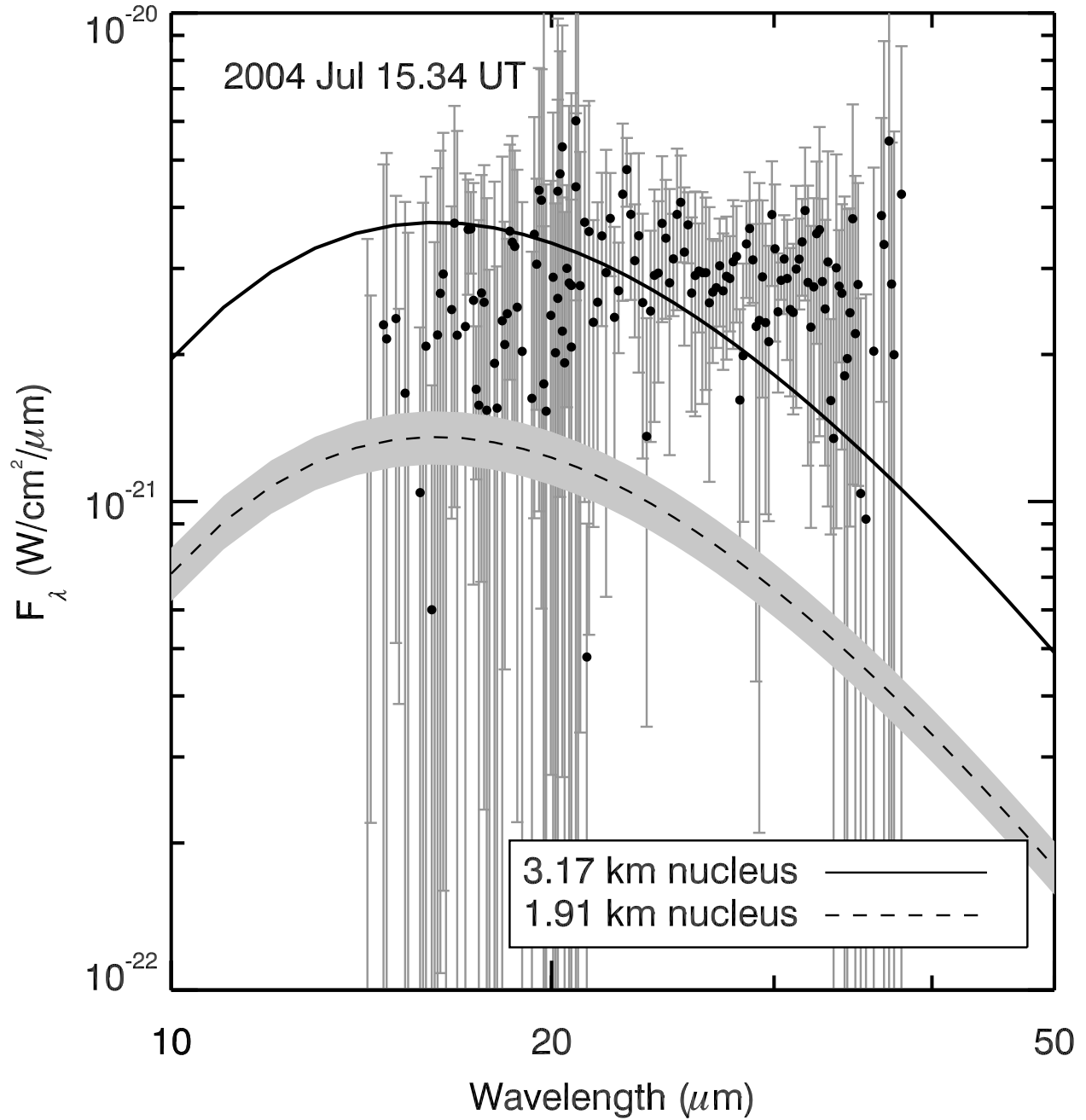


Fig. 11.— IRS spectrum of comet 67P/Churyumov-Gerasimenko and model nuclei. Only data points with a signal to noise greater than 0.5 are shown. The shaded area indicates the one standard deviation error on the nucleus size from Kelley et al. (2005a), $R = 1.91 \pm 0.09$ km.

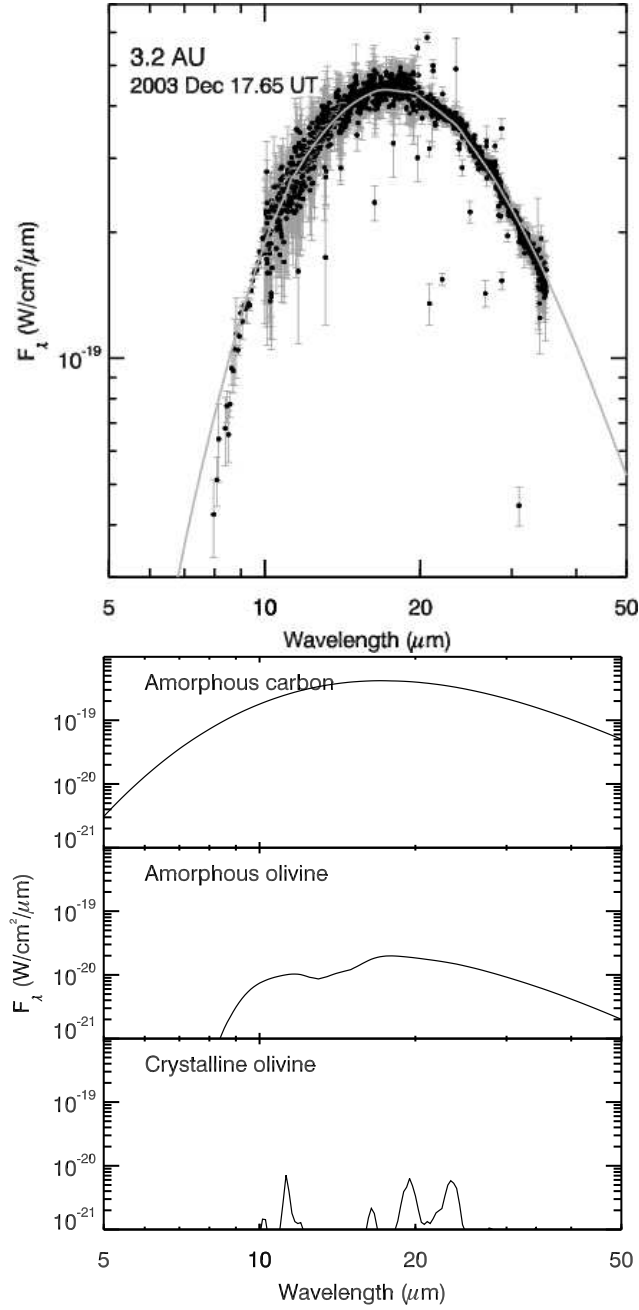


Fig. 12.— IRS spectrum of comet C/2001 HT50 (LINEAR-NEAT) at $r = 3.2$ AU and best-fit model of the dust thermal emission ($N = 4.2$, $M = 46.2$, $a_p = 1.2 \mu\text{m}$). Also shown are the decomposed spectra for each of the significant minerals in the best-fit model.

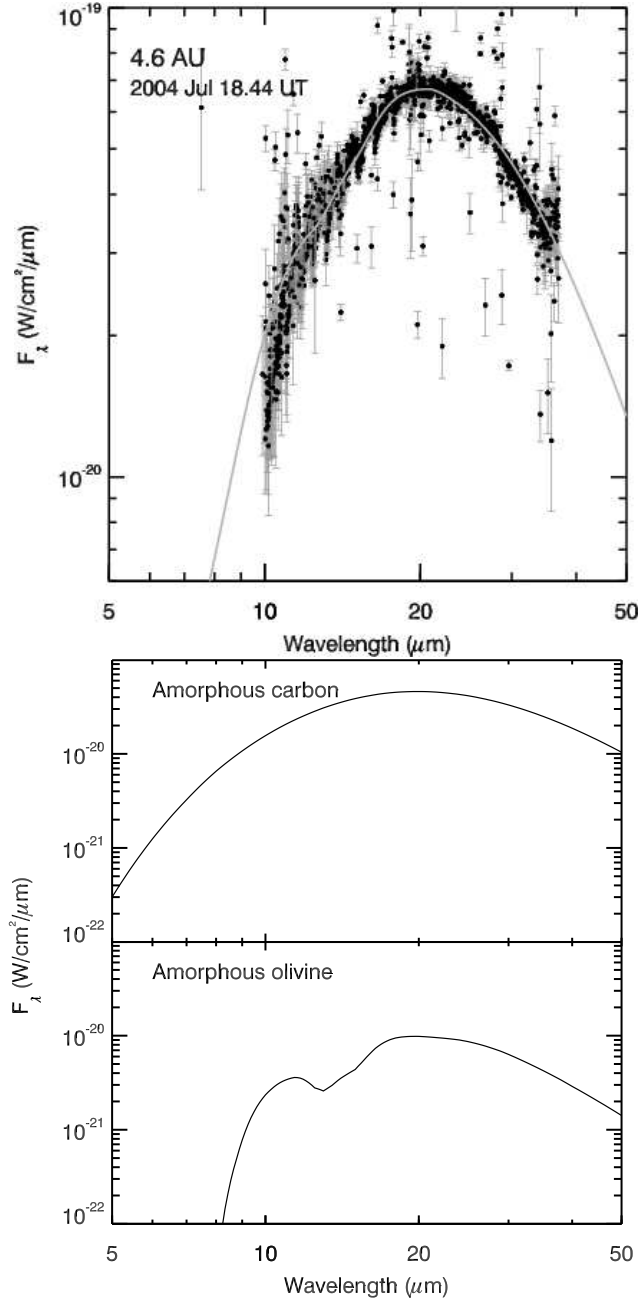


Fig. 13.— IRS spectrum of comet C/2001 HT50 (LINEAR-NEAT) at $r = 4.6$ AU and best-fit model of the dust thermal emission ($N = 3.7$, $M = 29.6$, $a_p = 1.2 \mu\text{m}$). Also shown are the decomposed spectra for each of the significant minerals in the best-fit model.

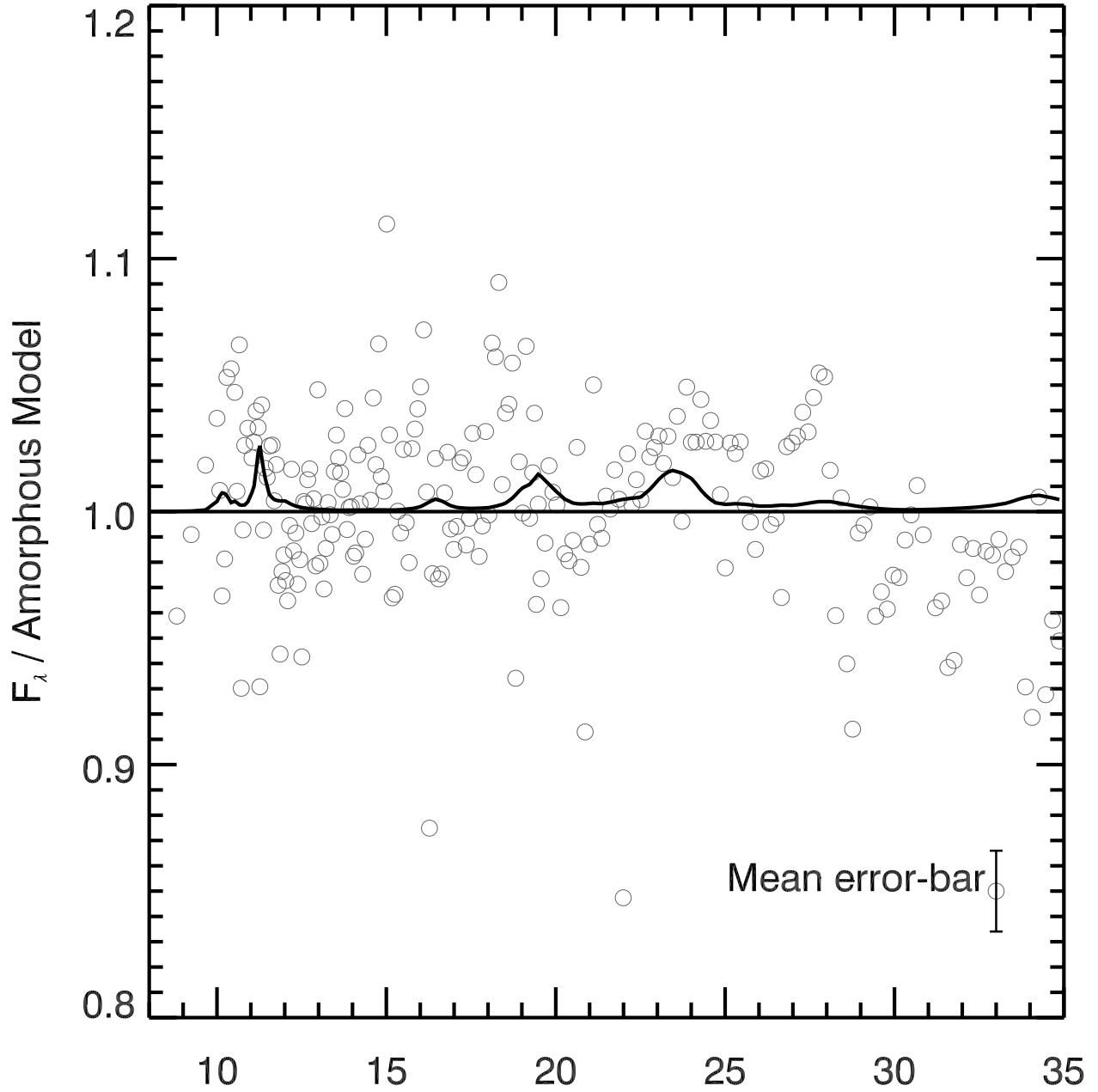


Fig. 14.— Spectrum of comet C/2001 HT50 (LINEAR-NEAT) at $r = 3.2$ AU binned by a seven-point statistically weighted, moving average and normalized by the sum of our amorphous mineral models (open circles); the solid line is the best-fit emission component from crystalline olivine dust. The presence of crystalline olivine as determined by the model appears to be driven by the shape of the spectrum at $23.5 \mu\text{m}$.

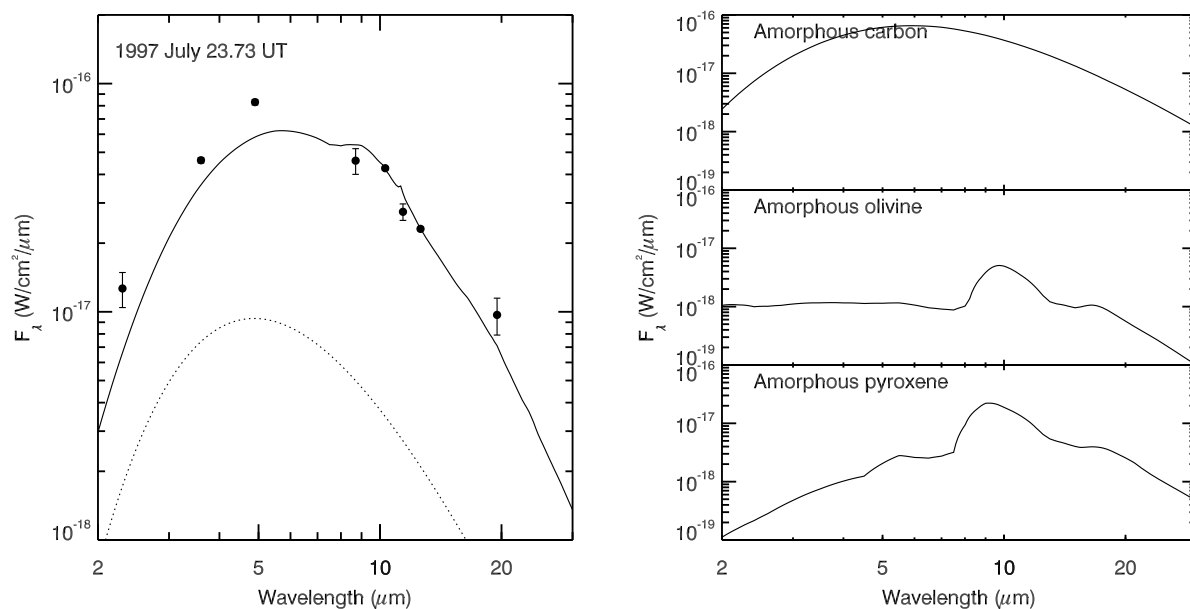


Fig. 15.— Comet 2P/Encke fluxes from 1987 July (Gehrz et al. 1989) and a model calculated from the *Spitzer*-derived coma mineralogy upper-limits (solid-line; Table 8) and the IRAC-derived nucleus parameters for $R = 2.34$ km at a phase angle of 63° (dotted-line; Table 6). The models are computed for the same viewing geometry as the photometer data ($r_h = 0.38$ AU, $\Delta = 1.13$ AU, $\phi = 63^\circ$). Also shown are the decomposed spectra for each mineral except crystalline olivine, which does not produce significant spectral features in the combined model (see §4.2).

Table 1. Slit widths and sizes of the constant width extraction apertures used for each module.^a

IRS Module	Slit Width (")	Aperture Width (")	Position Angle ^b (°)
SL	3.7	17.5	0
SH	4.7	11.3	-43
LL	10.7	51.5	-84
LH	11.1	22.3	-128

^aAdopted from the *Spitzer* Observers' Manual (Spitzer Science Center 2005) except SL and LL aperture widths (see §2.1). SL = short-low, 5–14 μm , $R \approx 64$ –128; SH = short-high, 10–20 μm , $R \approx 600$; LL = long-low, 14–38 μm , $R \approx 64$ –128; LH = long-high, 20–38 μm , $R \approx 600$.

^bRelative to SL (values from SPOT, <http://ssc.spitzer.caltech.edu/propkit/spot/>).

Table 2. Summary of comet spectroscopy.

Comet / Date (UT)	PID ^a	IRS Modules	Pre/Post- Perihelion	r_h^b (AU)	Δ_s^c (AU)	Phase Angle ^d (°)
2P/Encke						
2004 Jun 25.23	210	Red, SL, SH, LH	Post	2.573	1.985	21
2004 Jun 25.76	119	Blue, SL, LL	Post	2.577	1.982	21
67P/Churyumov-Gerasimenko						
2004 Jul 15.34	2316	Red, LL, LH	Post	4.978	4.743	12
C/2001 HT50 (LINEAR-NEAT)						
2003 Dec 17.65	131	Red, SL, SH, LH	Post	3.238	2.652	16
2004 Jul 18.44	131	Red, SL, SH, LH	Post	4.598	4.368	13

^a*Spitzer* Program ID

^bRed = 22 μm peak-up; Blue = 16 μm peak-up; SL = short-low, 5–14 μm , $R \approx 64$ –128; SH = short-high, 10–20 μm , $R \approx 600$; LL = long-low, 14–38 μm , $R \approx 64$ –128; LH = long-high, 20–38 μm , $R \approx 600$.

^c*Spitzer*-comet distance.

^dSun-comet-*Spitzer* angle.

Table 3. The parameters of third-order polynomial fits to the slit-loss correction factors versus wavelength (in units of μm).^a

Module	λ_0	λ_1	λ_2	λ_3
SL2	1.8591233	-0.3691497	0.0425228	-0.0017076
SL1	0.8424725	-0.0064947	-0.0006418	0.0000008
SH	0.6111256	0.0466900	-0.0040512	0.0000857
LL2	1.9293931	-0.1338932	0.0052684	-0.0000686
LL1	0.8016602	0.0051615	-0.0002820	0.0000017
LH	1.0151328	-0.0165096	0.0004606	-0.0000064

^aThe slit-loss correction factor spectrally calibrates extended sources of uniform surface brightness (see §2.1 and Fig. 1).

Table 4. Summary of comet 2P/Encke imagery.

Date (UT)	Wavelength (μm)	Pre/Post- Perihelion	r (AU)	Δ (AU)	Phase Angle ($^\circ$)
2003 Nov 11.73	3.6, 4.5, 5.8	Pre	1.094	0.232	63
2004 Jun 23.21	24, 70	Post	2.556	1.997	22
2004 Jun 29.92	3.6, 4.5, 5.8, 8	Post	2.611	1.958	20

Table 5. 2P/Encke color and aperture corrected nucleus fluxes.

Date (UT)	Wavelength ^a (μm)	Flux ($\text{W cm}^{-2} \mu\text{m}^{-1}$)
2003 Nov 17.75	3.55	$1.986 \pm 0.061 \times 10^{-18}$
	4.49	$5.06 \pm 0.11 \times 10^{-18}$
	5.73	$1.007 \pm 0.021 \times 10^{-17}$
2004 Jun 23.21	23.7	$2.30 \pm 0.24 \times 10^{-20}$
	71.4	$1.27 \pm 0.35 \times 10^{-21}$
2004 Jun 29.92	3.55	$7.0 \pm 2.8 \times 10^{-22}$
	4.49	$3.95 \pm 0.42 \times 10^{-21}$
	5.73	$1.07 \pm 0.11 \times 10^{-20}$
	7.87	$3.99 \pm 0.12 \times 10^{-20}$

^aIRAC or MIPS effective wavelengths.

Table 6. 2P/Encke NEATM fit to the 2004 June and 2003 November data^a.

Parameter	2004 June	2003 November	
		Fixed η	Fixed R
radius, R (km)	2.34 ± 0.14	1.72 ± 0.10	2.34
geometric albedo, p_v	0.047	0.047	0.047
IR beaming parameter, η	0.735 ± 0.046	0.735	1.026 ± 0.061
IR emissivity, ϵ	0.9	0.9	0.9
reflected light scale, α	0.047 ± 0.027	0.031 ± 0.022	0.127 ± 0.016
degrees of freedom, ν	3	1	1
χ^2_ν	3.5	11.6	0.11

^aValues without error bars are fixed parameters.

Table 7. Scaling factors for each extracted spectrum.^a

Comet	SL	SH	LL	LH
2P/Encke (SL+LL)	1.53	...	1.30	...
2P/Encke (SH+LH)	...	0.48	...	0.58
C/2001 HT50 (LINEAR-NEAT) (3.2 AU)	1.24	1.00	...	1.51
C/2001 HT50 (LINEAR-NEAT) (4.6 AU)	1.81	1.00	...	1.23

^aThe spectrum of comet 67P/Churyumov-Gerasimenko was not scaled.

Table 8. Comet 2P/Encke best-fit thermal emission model parameters.

Data	N	M	a_p^a (μm)	D^b	N_p ($\times 10^{18}$)				ν	χ_ν^2
					Amorphous Carbon ^c	Amorphous Olivine	Amorphous Pyroxene	Crystalline Olivine		
SL+LL	3.7	11.1	0.4	2.857	$2.38 \pm \begin{smallmatrix} 0.12 \\ 0.17 \end{smallmatrix}$	<0.14	<0.77	<0.07	240	0.97
SH+LH	3.7	11.1	0.4	2.857	$2.54 \pm \begin{smallmatrix} 0.06 \\ 0.17 \end{smallmatrix}$	<0.03	<0.44	<0.10	1473	0.47

^aOur estimated error in a_p is $0.05 \mu\text{m}$ (see §3.1.2).

^bFractal dimension of the amorphous components; crystals always have a fractal dimension of 3.0 (i.e., solid grains).

^cAmorphous carbon represents the warm, deeply absorbing component in comet dust.

Table 9. Comet C/2001 HT50 (LINEAR-NEAT) best-fit thermal emission model parameters.

Date (UT)	r (AU)	N	M	a_p^a (μm)	D	N_p ($\times 10^{19}$)				ν	χ_ν^2
						Amorphous Carbon	Amorphous Olivine	Amorphous Pyroxene	Crystalline Olivine		
2003 Dec 17.65	3.2	4.2	46.2	1.2	3.000	$3.12 \pm \begin{smallmatrix} 0.03 \\ 0.13 \end{smallmatrix}$	$0.12 \pm \begin{smallmatrix} 0.10 \\ 0.03 \end{smallmatrix}$	<0.03	$1.27 \pm \begin{smallmatrix} 0.86 \\ 0.32 \end{smallmatrix}$	1686	4.2
2004 Jul 18.44	4.6	3.7	29.6	1.2	2.857	$2.98 \pm \begin{smallmatrix} 0.61 \\ 0.03 \end{smallmatrix}$	$0.49 \pm \begin{smallmatrix} 0.73 \\ 0.09 \end{smallmatrix}$	<0.85	<3.4	1690	23.8

^aOur estimated error in a_p is $0.05 \mu\text{m}$ (see §3.1.2).

Table 10. Relative mineralogy of comets 2P/Encke and C/2001 HT50 (LINEAR-NEAT) by mass of sub-micron grains derived from Tables 8 and 9^a .

Comet	r (AU)	Amorphous Carbon	Amorphous Olivine	Amorphous Pyroxene	Crystalline Olivine	Silicate / Carbon
2P/Encke ^b	2.6	$1.00 \pm \begin{smallmatrix} 0.00 \\ 0.07 \end{smallmatrix}$	<0.01	<0.14	<0.05	<0.08
C/2001 HT50 (LINEAR-NEAT)	3.2	$0.63 \pm \begin{smallmatrix} 0.01 \\ 0.05 \end{smallmatrix}$	$0.032 \pm \begin{smallmatrix} 0.012 \\ 0.004 \end{smallmatrix}$	<0.006	$0.34 \pm \begin{smallmatrix} 0.05 \\ 0.02 \end{smallmatrix}$	$0.59 \pm \begin{smallmatrix} 0.14 \\ 0.04 \end{smallmatrix}$
C/2001 HT50 (LINEAR-NEAT)	4.6	$0.82 \pm \begin{smallmatrix} 0.04 \\ 0.25 \end{smallmatrix}$	$0.18 \pm \begin{smallmatrix} 0.11 \\ 0.08 \end{smallmatrix}$	<0.14	<0.60	<2.2
C/1995 O1 (Hale-Bopp) ^c	2.8	0.11	0.18	0.18	0.48	8.1
9P/Tempel 1 (pre- <i>DI</i>)	1.5	0.0	1.0	0.0	0.0	...
9P/Tempel 1 (<i>DI</i> +1.0) ^d	1.5	0.21	0.27	0.41	0.10	3.7

^aIncluded for comparison are comets C/1995 O1 (Hale-Bopp) and 9P/Tempel 1 pre- and post-*Deep Impact* encounter (Harker et al. 2004, 2005).

^bValues derived from the SH+LH model fit of Table 8.

^cThe remaining 5% is composed of orthopyroxene.

^dTime of impact +1.0 hour.